POLITECNICO DI TORINO

Master's degree program

Energy and Nuclear Engineering

Master Thesis

Numerical modelling of a thermocline energy storage system with internal electric resistances for CSP and PV hybrid plant

Tutors:

Prof. Roberto Zanino

Dr. Mattia Cagnoli

Candidate:

Aleksandra Milic

S301455

a.y. 2023/2024

Table of Contents

Abstract

With the growing concerns regarding climate change and the need to move towards sustainable energy sources and stable energy supply, energy storage systems have become one of the main focuses of research. This thesis addresses this issue through the numerical modelling of a single-tank thermal energy storage system (TES) integrated with internal electric resistances, designed for Concentrated Solar Power (CSP) and Photovoltaic (PV) hybrid plants. This research is done as a part of an ongoing project of the Italian National Agency for New Technologies, Energy, and Sustainable Economic Development (ENEA).

The introduction describes the main environmental and technical issues that the energy sector faces. Additionally, in this paragraph main aspects relevant to this research are explained, including ways of harnessing solar energy, the benefits of hybridization, as well as principles of energy storage systems, with a focus on thermocline systems. Following that, the theoretical framework explores the principles of thermal fluid dynamics and natural convection, offering the understanding necessary for the development of numerical models.

The central focus of this study lies in the development and validation of a numerical model for the thermocline energy storage system. The methodology includes benchmark case validation, a description of the computational domain with boundary conditions, grid and timestep independence studies, as well as a parametric study for the improvement of heat transfer characteristics of the electric heater for two different heater configurations. All simulations are performed in STAR-CCM+, Computational Fluid Dynamics (CFD) software by Siemens.

Results consist of a comparative analysis between two different electric heater models, highlighting the advantages and potential of each heater configuration. For configuration that shows better potential, control of charging mass flow rate was carried out to get the constant temperature charging, and good thermocline layer. Additionally, as a reference solution, the model was simulated with constant mass flow rate charging. Based on the results of the simulations, perspectives for future research for the improvement of mass flow rate control were proposed.

1. Introduction

Following the growing concerns about climate change and its effects on the environment and the future survival of the world as we know it, the development of different renewable energy systems becomes a crucial pathway for reaching sustainability in the energy sector. Besides the environmental aspect, sustainability refers also to financial stability and resource utilization, as well as diverse social issues. The need to consider all its aspects in current and future projects has led to the development of various energy-efficient systems, and one example of that is hybrid plants. Hybridization enhances the system efficiency, contributes to energy security and level of resource usage, and reduces the overall normalized cost of the system, which makes it more financially viable compared to individual systems. However, to optimize the advantages of hybridization, new technical solutions need to be developed. This thesis focuses on the modelling of the internal electrical heating elements of a thermal energy storage system. This allows the introduction of a photovoltaic (PV) field to an existing concentrated solar power system (CSP) and makes the energy storage unit a connecting element of the hybridization.

This paragraph explains the importance of decarbonization of the energy industry, the tendencies, and trends in this sector, and introduces the problem of the following work.

1.1 Climate change

The term *climate change* refers to the ongoing increase in the average global temperature – *global warming*, and its effects on the environment. It is predominantly driven by human activities and the industrialization of society, which caused the increase in the emission of greenhouse gases that trap the heat in the atmosphere. These changes impact ecosystems, biodiversity, and societies, with profound consequences for agriculture, water resources, sea levels, and overall environmental stability.

1.1.1 Greenhouse gas (GHG) emissions

The concentration of some gases in the atmosphere causes the temperature disbalance. When solar radiation reaches the surface of the Earth, some of its energy is absorbed which warms the ground and some is reflected to space. Greenhouse gases that are in the atmosphere re-emit some of this radiation back towards the Earth which captures the heat that would otherwise go back to space (Figure 1.1). Without this effect, life on Earth wouldn't be possible, because it secures the right temperature for life (average temperature between the freezing and boiling temperature of water) [1]. However, the increased concentration of these gases caused by emissions from industrial facilities has increased the average temperature by 1.1℃ compared to the pre-industrial era (*source: IPCC*). Scientists predict that without taking action to stop this increase, it could get to the values fatal for life on Earth.

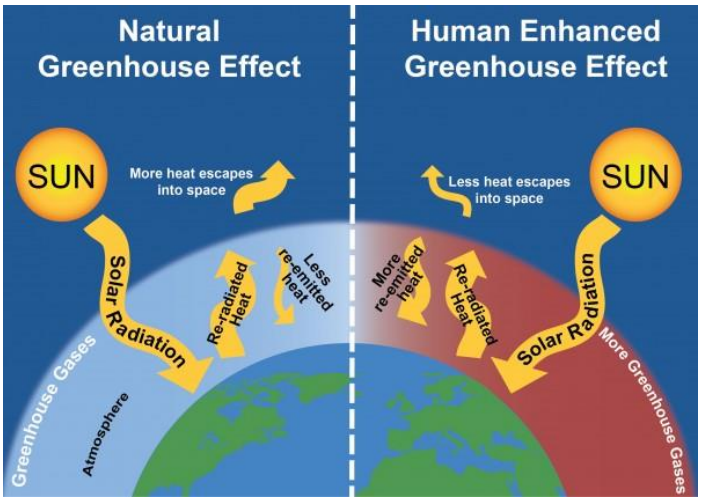

FIGURE 1.1: GREENHOUSE EFFECT (SOURCE: CSS.SNRE.UMICH.EDU)

The main GHGs are:

- Carbon dioxide (CO_2) – the increase in the concentration of this gas in the atmosphere compared to pre-industrial era is 40%; responsible for 20% of thermal absorption
- Methane (CH_4) – its concentration is only 0.5% that of CO_2, but it is 30 times more powerful as GHG, which causes concerns for future
- Nitrous Oxides (N_xO) – as GHG N_2O is 300 times stronger than CO_2
- Water Vapor – water vapor and clouds are responsible for most of the thermal absorption, but the atmospheric lifetime of water is short compared to other GHGs

1.1.2 Effects on nature and health

The impacts of climate change on the environment are diverse and frequently interconnected, affecting ecosystems, weather, social and economic stability, and ultimately human well-being. Here are some key effects [2]:

- **Temperatures:** Nine warmest years on record since 1880 have all occurred in the period between 2014-2022 (data from 2022 report). The average global temperature has been rising at a rate of 1.7℃ per century, which is significantly higher than the 0.01℃ rate over the past 7,000 years.
- **Extreme weather conditions:** An increase in the frequency and intensity of extreme conditions such as floods, wildfires, droughts, and hurricanes has been closely associated with climate change, as well as hot and cold extreme temperature occurrences.
- **Sea level:** Global mean sea level has rose between 15 and 25 cm since 1901, due to deep ocean warming and ice sheet melting. In 2022, annual arctic temperature increased by 0.73℃ compared to the average temperature of 30 previous years.
- **Ecosystems:** Weather changes cause species migrations. Approximately half of the species have shifted to higher elevations or towards the poles. The acidity of the oceans has increased, as the ocean absorbs about 31% of industry-caused CO_2 emissions, and this change has affected marine life. Climate change is also a major driver of the loss of biodiversity, because of the inability of certain species to adapt quickly to changes in the ecosystem.
- **Food and water resources:** Temperature changes can affect the crop yields and productivity of agricultural systems. Water resource degradation has been closely related to temperature changes. Food and water scarcity can have great social and economic consequences.
- **Health:** Air and water quality have a great impact on human health. The occurrences of food-borne and water-borne diseases have increased. Besides the changes related to global warming and CO_2, high levels of air pollution caused mainly by particulate matter emissions can increase the risk of respiratory system diseases and infections, as well as neurological, cardiovascular, reproductive, and immune system damages.

1.1.3 The main causes of GHG emissions

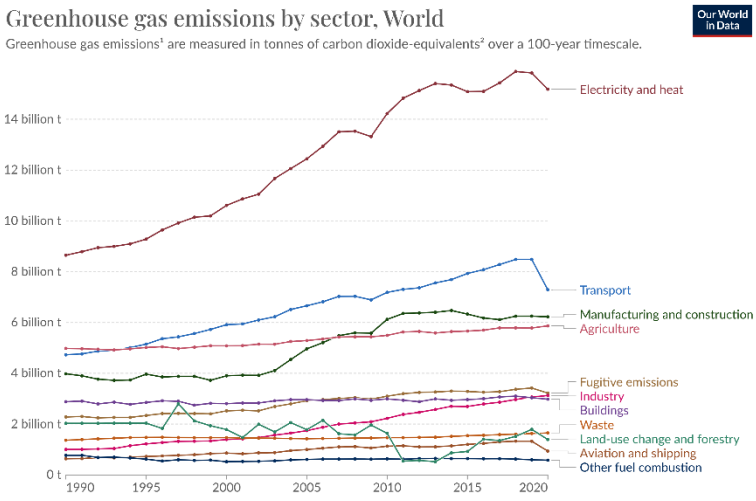

FIGURE 1.2: GLOBAL GHG EMISSIONS BY SECTOR OVER THE YEARS [3]

Carbon dioxide emissions can be caused by both natural and human factors. Natural phenomena, such as volcano eruptions, wildfires, and decomposition of organic matter, emit large amounts of CO_2, but their contributions are generally in equilibrium with natural carbon sinks (forests, oceans, soils...). The cause of the disbalance in the carbon cycle are the CO_2 emissions from various industry sectors. As seen on Figure 1.2, the biggest emitter of greenhouse gases is the energy sector, with electricity and heat production as the main source of equivalent CO_2 emissions. The reason is that most of the electricity and heat production in the world comes from fossil fuel (coal, oil and natural gas) combustion. That's why the imperative for dealing with climate change is moving the energy production to renewable energy resources.

1.1.4 Sustainability

Sustainable development refers to a careful utilization of existing resources to meet the needs of the present consumption, without compromising the ability of future generations to meet their own needs. The global energy demand needs to overcome two main challenges: the environmental effect of fossil fuel combustion in energy generation, and scarcity of fossil fuel resources. Both challenges lead to a conclusion that energy needs to shift its production towards renewable energy sources.

To fight global social, economic and environment challenges, the *United Nations* has set 17 Sustainable Development Goals (SDG) which provide targets to be achieved by 2030, indicators based on which we can measure the improvement, and global actions showing the way to achieve the set targets [4]. For energy sector, following goals are the most important:

- **SDG 7: Affordable and clean energy** – sustainably increasing the share of renewable energy in the global energy mix, by not disrupting energy security and reliability, making energy more financially and geographically affordable, reachable, and clean, and improving the energy efficiency.

- **SDG 13: Climate action** – sets the base for research, education, awareness raising, strategies and planning for climate change impact reduction.

To reach these goals, the energy sector needs to work on the development and implementation of new renewable energy technologies, to overcome the technical challenges that come with it (further explained in paragraph 1.2.2). Besides the environmental aspect, energy transition towards renewables needs to consider also economic and social factors.

1.2 Decarbonization of the energy sector

As it was explained in the previous paragraph, the energy sector aims to transition from predominantly fossil fuel production to more sustainable energy sources, like renewables and nuclear energy. This paragraph introduces different types of renewable energy sources, as well as technical obstacles that production from these sources faces. Ways to overcome these challenges, research objectives, and trends in the energy sector can be found in paragraph 1.2.3.

1.2.1 Renewable energy sources

Renewable energy sources (RES) harness natural phenomena to generate electricity or heat, with minimal or no emissions of harmful gases to the environment. Compared to fossil fuels reserves that are distributed unevenly on Earth and decreasing in availability, most renewable sources are practically inexhaustible and widely accessible globally. The key types of renewables are:

- **Solar energy** – converts sunlight to electricity or heat by using photovoltaic or solar thermal systems (paragraph 1.3)
- **Wind energy** – converts wind's kinetic energy to electricity by using wind turbines. They can be placed on the land (onshore) or in the sea/ocean (offshore), and they can produce significant amounts of electricity. The wind plants can cause a negative effect to the environment by forcing the migrations of bird and marine life species and producing noise.
- **Biomass energy** – uses organic materials such as agricultural residues or organic waste, to produce electricity, heat, or biofuel. Biomass combustion produces emissions, so it must be sourced sustainably to ensure minimal impact on the environment. Biofuels have a great potential for becoming important fuel for transportation, replacing diesel and gasoline.
- **Hydropower** – uses the kinetic and potential energy of water flows and reservoirs for electricity production and storage. This is the oldest and most widely used renewable energy resource. The effect of these plants on the neighboring ecosystem needs to be analyzed and minimized during the design process.
- **Ocean energy** – uses the kinetic energy of waves and tides to produce electricity. This is relatively new technology, and many projects are in the early stages of development. However, ocean energy offers significant potential in electricity production. The effects on marine life are still being researched.
- **Geothermal energy** – uses the heat of Earth's interior for heating and cooling systems, and electricity generation. This form of energy is constant, so it can be used to provide baseload power.

Each of the renewable energy resources has its advantages and challenges. Future energy systems are projected to have a balanced mix of all or most RES power plants, to enhance energy security and reliability.

1.2.2 Intermittency of renewables

One of the biggest challenges for most RES is their intermittent nature. Solar, wind, and ocean energy resources cannot be controlled in frequency or intensity. Luckily, statistical analyzes of their occurrences over significant periods of time can be used to forecast their future behavior with sufficient preciseness, providing reliable data for project designs.

To keep a stable and reliable supply of energy, it's essential to monitor and predict electricity and heat demand fluctuations in real-time. These variations in the demand are caused by many factors, such as: time of the day (with lowest demand typically occurring during the

night), period of the year (with peak demand often in winter), special events (resulting in increased demand during holidays), weather and economic conditions, etc. Recognizing that factors impacting energy demand are rarely in any correlation with renewable energy sources occurrences, it becomes evident that relying solely on solar, wind, and ocean energy, despite their significant potential, would not enable us to meet energy demand in real-time (Figure 1.3). Additionally, while weather forecasts can offer accurate estimates of average values over extended periods, their precision diminishes for minute-to-minute predictions. Therefore, planning energy supply for shorter timeframes, such as daily or hourly, cannot be achieved with sufficient certainty.

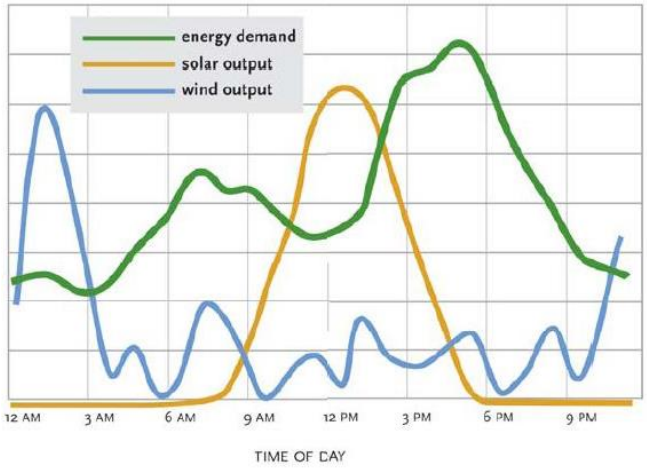

FIGURE 1.3: EXAMPLE OF DAILY ENERGY DEMAND AND RESOURCES FLUCTUATIONS [5]

The solution to the intermittency obstacle would be introduction of systems that could take the surplus energy from the grid during periods of excess production, keep it and give it back to the grid when the demand surpasses production levels. These systems are called energy storage systems (more details in paragraph 1.5).

1.2.3 Trends in the energy sector

For total decarbonization of the energy sector, it is necessary to replace fossil fuel-based energy production with renewable and nuclear energy resources. The problem of the intermittency of the renewable sources that show the greatest potential for baseload generation (solar and wind) is the main obstacle this sector is facing. Meeting energy demands requires the grid to constantly provide baseload power, and additional fluctuating power. Neither solar nor wind energy can be harnessed continuously during the day, season, or year. Fortunately, the occurrence of these two forms of energy is complementary (Figure 1.4). Therefore, developing solar and wind systems coupled with energy storage units for flattening the

production curve presents a promising option for future energy systems. This represents one of the primary areas of focus in current energy sector research.

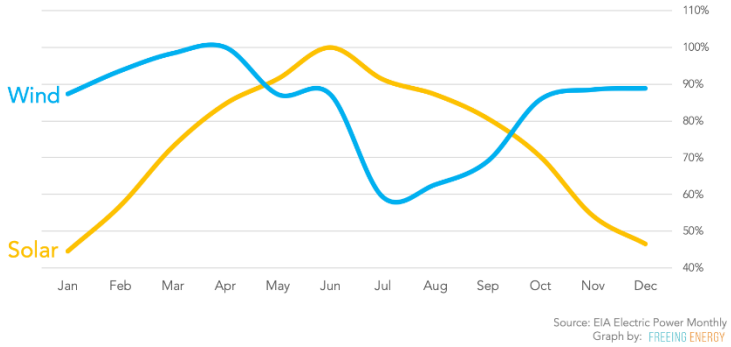

FIGURE 1.4: EXAMPLE OF SEASONAL OCCURRENCES DIFFERENCE BETWEEN WIND AND SOLAR ENERGY

Solar and wind energy have made a significant contribution to energy production over time. As technology develops and becomes more widely adopted, its cost decreases. The Levelized Cost of Energy (LCOE) is a parameter that indicates the average cost of each kWh produced by the analyzed system, including both investment and maintenance costs of the plants throughout its operational lifespan. It is a useful tool for comparing different technologies. Figure 1.5 illustrates the changing of average global LCOE for solar and wind technologies over the years. The dotted lines represent the range of LCOE for fossil fuels energy production technologies. Solar and wind technologies have already achieved financial competitiveness with fossil fuels, with photovoltaics and onshore wind plants already surpassing them. This means that building a new RES plant is increasingly more affordable than a new fossil fuel plant, which is a great opportunity for greener production even from a financial perspective. Additionally, LCOE for concentrated solar technologies is more than twice as high as that of photovoltaic technology. Adding a photovoltaic field to the concentrated solar plant decreases its cost.

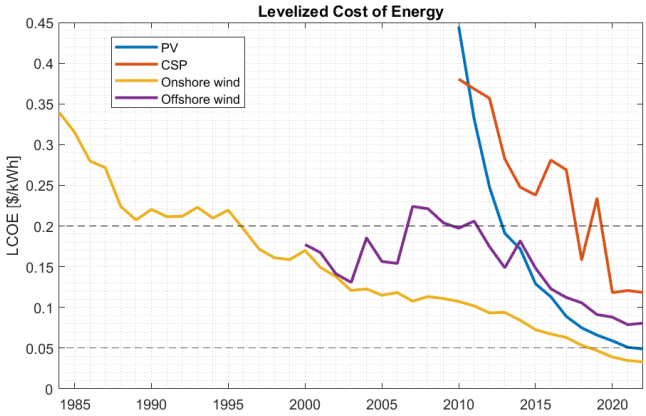

FIGURE 1.5: AVERAGE GLOBAL LCOE THROUGH THE YEARS FOR DIFFERENT RES [6]

1.3 Solar energy

The total solar energy that reaches Earth's surface in just one hour is enough to fulfill global energy needs for an entire year. Therefore, this form of energy is practically inexhaustible and additionally, it is free, so in the process of using solar energy for electricity or heat production, we don't have maintenance costs related to resource purchase, making it cost-effective. With the construction of solar plants, countries can reduce the dependence of energy on fossil fuel import issues, enhancing energy security.

Two ways for utilization of solar energy for electricity and heat generation are installation of Photovoltaic (PV) panels and solar-thermal energy conversion technologies, such as Concentrated Solar Power (CSP).

1.3.1 Photovoltaic plants

Photovoltaic plants are constructed out of solar panels that directly convert solar energy into electricity. The technology of this conversion is based on the photoelectric effect, which describes how the energy of photons is transferred to kinetic energy of electrons in semiconductor materials and metals – creating electric current (Figure 1.6).

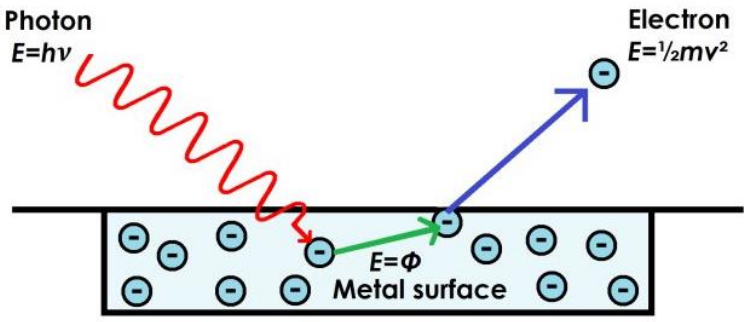

FIGURE 1.6: PHOTOELECTRIC EFFECT (SOURCE: SCIENCEANDSF.COM)

Solar panels have become widely used globally, as their price has significantly decreased in the last two decades. The challenge remains the intermittent occurrence of solar energy, and therefore intermittent electricity production. To achieve autonomous electricity production from solar panels, they are usually paired with batteries for energy storage. This type of energy storage increases drastically the investment cost of the entire system, and, since the batteries lifespan is much shorter than the lifespan of solar panels, it also increases the maintenance costs related to frequent batteries replacement.

1.3.2 Concentrated Solar Power plants

Concentrated Solar Power is a type of solar-thermal technology. Using mirrors or lenses (collectors), solar radiation that falls on big surfaces is reflected, and large amounts of thermal energy are thus concentrated onto a small area (receiver). This thermal energy is then used to heat a fluid (oil, water, molten salts) inside a receiver which, in most cases, is later used for charging thermal energy storage. Energy storage is being discharged in an Organic Rankine Cycle (ORC) whose product is electricity (Figure 1.7).

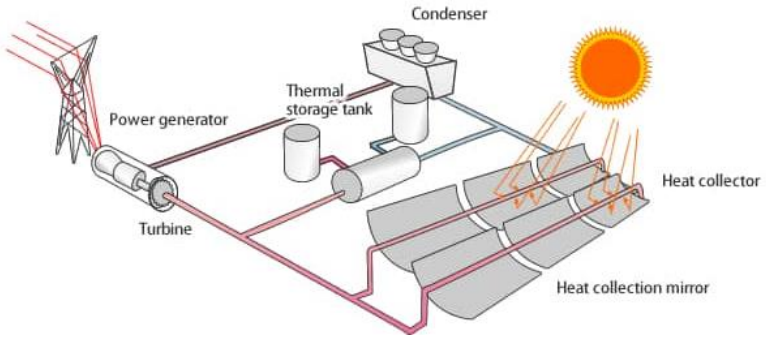

FIGURE 1.7: CSP SYSTEM SCHEMATIC

Depending on the type of concentration technology, CSP plants can be constructed with either line receivers or point receivers. All types of concentrated solar collectors must be equipped with an automation system that tracks the Sun's position during the day. Considering line receivers (tubes with heat transfer fluid flowing inside), we can distinguish two main types of collectors:

- **Parabolic troughs**: this technology uses large mirrors whose cross section is in the shape of parabola, which allows all the sunlight that falls on its surface to be reflected in one line, which is the focal point of each cross section (Figure 1.8)
- **Linear Fresnel**: this technology uses a set of mirrors placed in a way that imitates the Frensel lens optical characteristics. This way, rays of sunshine that fall on the surface of the mirrors still reflect in the same focal point (with lower energy yield per surface compared to parabolic troughs), but the production cost of the mirrors is reduced (Figure 1.9)

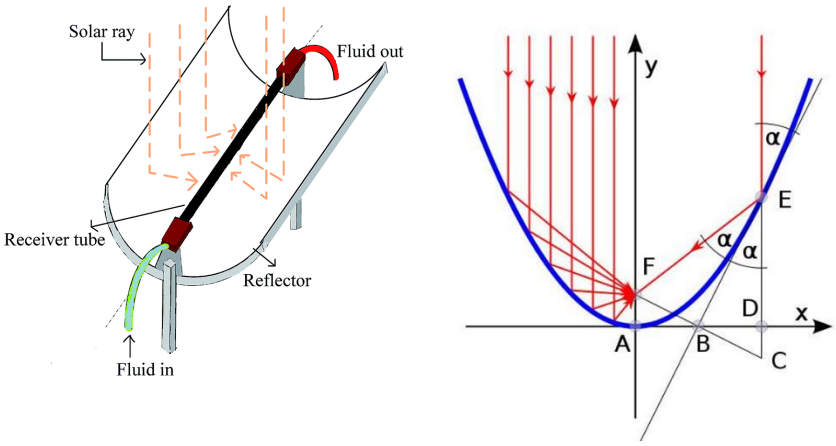

A) B)

FIGURE 1.8: PARABOLIC THROUGH A) SYSTEM DIAGRAM B) CROSS SECTION REFLECTION

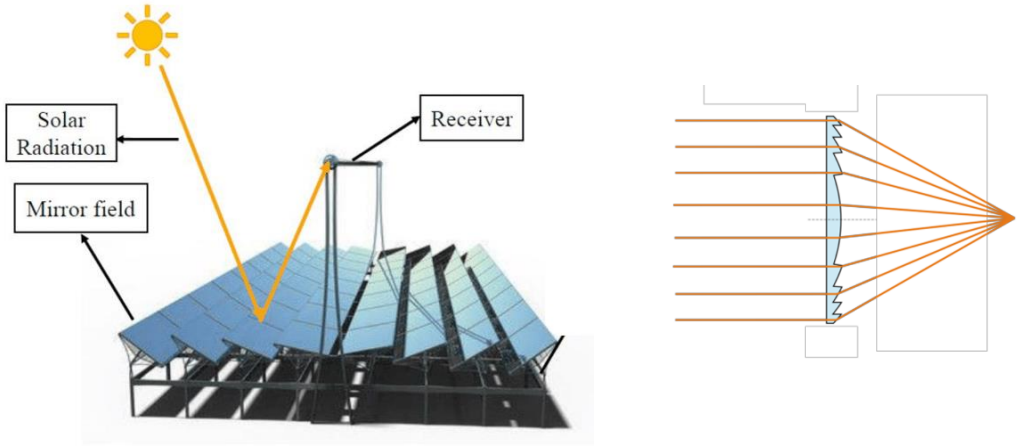

A) B)

FIGURE 1.9: A) LINEAR FRESNEL SYSTEM DIAGRAM B) FRESNEL LENS OPTICS

Regarding point receivers, there are two main collector types:

- **Solar towers (Central Receiver System)**: this technology uses a large array of mirrors (heliostats) that reflect sunlight in one point receiver at the top of a tower (Figure 1.10). Every mirror needs to be tilted in a precise way so that it correctly aims at the point receiver, and this complicates the tracking system.

A) *B)*

FIGURE 1.10: SOLAR TOWER SYSTEM A) WORKING PRINCIPAL B) DESIGN EXAMPLE

- **Dish Stirling**: this technology uses a large dish-shaped mirror to concentrate sunlight onto a receiver located at the focal point of the dish (Figure 1.11). There is a Sterling engine inside the receiver that transforms thermal energy into mechanical energy, which is later converted to electricity.

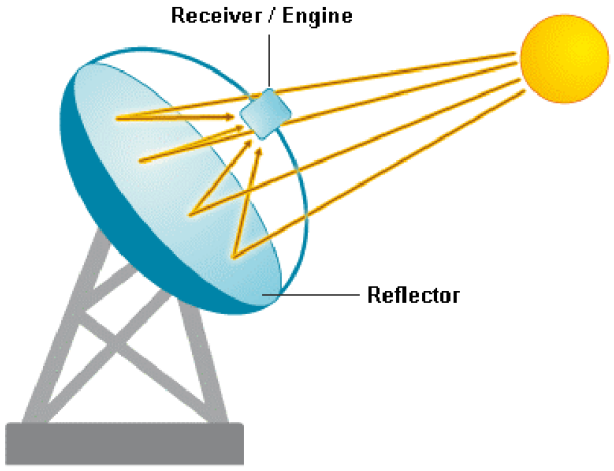

FIGURE 1.11: DISH STIRLING SYSTEM DIAGRAM

1.3.3 CSP and PV hybrid plant

From the previous paragraph, we can see that the product of concentration of solar energy is thermal energy. This makes it easy, and economically viable, for CSP plants to integrate thermal energy storage that allows the system to produce electricity independently of the solar irradiation during the day. From paragraph 1.2.3 it can be noticed that photovoltaic systems have reached a point of low Levelized Cost of Energy, because of their low installation and maintenance cost, unlike CSP technologies that are still developing. Therefore, the hybridization of these two solar systems can provide an energy storage unit for intermittent PV generation and at the same time can lower the CSP technology LCOE [7].

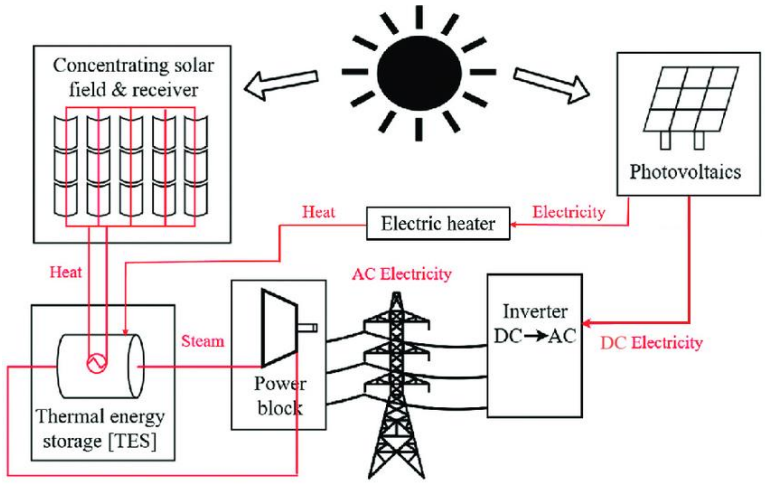

FIGURE 1.12: DIAGRAM OF THE HYBRID CSP AND PV SYSTEM

The integration of these two systems is done by the adaptation of a thermal energy storage (TES) system (Figure 1.12). Both systems use solar radiation as their energy source. CSP part of the plant concentrates the solar energy onto the tube receivers (in this case we have a line receiver system), and as a product we have a thermal energy that heats the heat transfer fluid inside the receiver. These tubes are connected to the heat exchangers inside the thermal energy storage tank, and the heat from the solar field is thus transferred to the storage medium. TES is later discharged by the Organic Rankine Cycle which uses the thermal energy of the storage to form high-temperature steam which powers the turbine, thus transforming thermal energy into mechanical. The turbine is connected to a generator that converts mechanical energy into electricity. On the other hand, in the photovoltaic part of the plant, we have a direct conversion of solar energy into electricity. Therefore, during the operational hours when sunlight is available, the electricity from the PV field can be supplied to the grid. Alternatively, if the market price of the electricity is unfavorable, this surplus energy can be used to heat the TES, and it can be stored. To convert the electricity to thermal energy, an additional element is required, such as an electric heater. This heater can either indirectly heat the transfer fluid that

heats the storage medium via heat exchanger, or it can be immersed inside the thermal storage unit, heating the storage medium directly.

1.4 Energy storage

Because of the intermittent nature of renewable energy sources, energy storage systems have a crucial role in their integration into the electricity grid. Its purpose is to store surplus energy produced by RES in hours of low electricity demand, and high production, and inject it back into grid during hours of peak electricity demand or when the renewable resource is not available. The green part of the graph in Figure 1.13 represents the excess electricity produced by the solar system, that once stored can be utilized to meet electricity demand in the nighttime hours. Energy can be conserved in different forms, but the energy storage system must be compatible with the resource, to achieve more energy-efficient and cost-effective solutions.

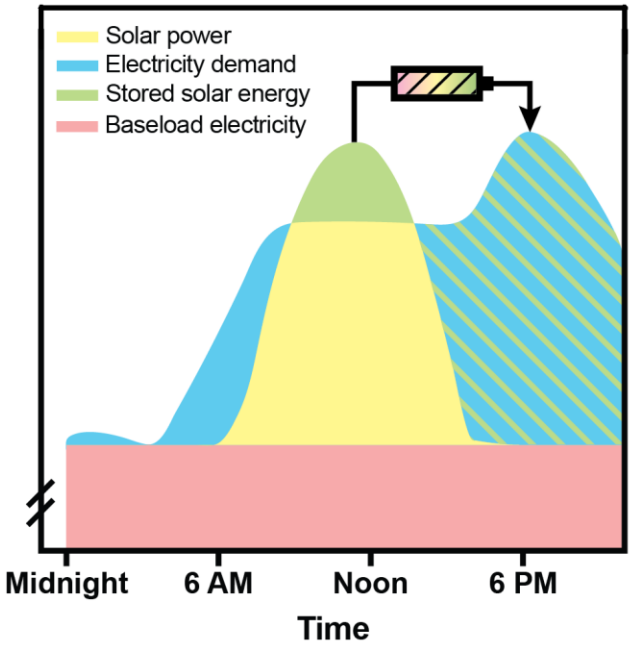

FIGURE 1.13: STORING SOLAR ENERGY (SOURCE: SINT.HMS.HARVARD.EDU)

1.4.1 Types of energy storage

The main types of energy storage, some already in use, some in developing process are:

- **Thermal energy storage (TES)** – thermal energy is stored in well-insulated tanks, and it is later used in thermodynamic cycles to produce electricity. It can be sensible storage, which is related to temperature difference of the liquid or solid material that fills the storage unit, or latent storage, that is associated with the phase change of the material.
- **Rechargeable batteries** – convert electricity into chemical energy, that can be converted back to electricity. They are often used for autonomous photovoltaic systems, because of the nature of the full charging-discharging cycle that includes conversion of electricity to only one other form of energy.
- **Pumped-storage hydroelectricity** – in hydropower plants, the energy can be stored in the form of potential energy, by pumping the water to the higher elevation during the overproduction and releasing that water back to the lower elevation to drive a turbine and produce electricity. This is one of the oldest types of energy storage systems. It is suitable for large scale storage, and it has a long lifespan.
- **Compressed air energy storage** – storage is charged by compressing air into underground reservoirs, and it is expanded back for discharging.
- **Flywheels** – energy is stored in the form of kinetic energy that spins the rotor at high speeds. Suitable for short-term storage solutions.
- **Hydrogen** – production of hydrogen through electrolysis that uses the surplus electricity from the grid. This hydrogen can later be used for fuel cells, or combustion engines to produce heat and electricity.

1.4.2 Thermocline TES

Thermal energy storage (TES) systems allow CSP plants to have electricity generation independent of sunlight availability. Thermal energy from the CSP field is transported with heat transfer fluid (HTF) to the heat storage medium (HSM) that fills the TES. Depending on the materials used for HTF and HSM, there are many different types of TES [8]. HSM can be a solid material, with examples like concrete block, fluidized or moving bed [9], a combination of solid and liquid materials, like packed bed systems [10], or just liquid materials.

Regarding liquid materials for thermal storage, compared to oil or water, using molten salt as the HSM allows energy conservation at much higher temperatures, which corresponds to higher energy efficiency of electricity generation. Additionally, volumetric heat capacity of molten salt is much higher than of the other liquids used in this application, which allows construction of smaller storage units for the same energy storage capacity.

Conventional design of the TES for CSP application consists of two tanks: one with molten salt at a high temperature (hot tank), and the other at lower temperature (cold tank). The HTF (that can be the same as HSM or different, depending on whether the storage is direct or indirect) flows from cold tank, absorbs heat from the CSP field, and is then stored in the hot tank. During discharging, the flow direction is reverse.

Another solution for thermal storage is a single-tank configuration. This tank contains both high temperature fluid and low temperature fluid (Figure 1.14). Driven by buoyancy forces, hot temperature fluid is concentrated on the top of the tank, while cold fluid remains at the bottom. The two parts are separated by thermocline region, that represents the temperature stratification. The charging heat exchanger is supposed to be placed closer to the bottom of the tank, to achieve better heat transfer, since this way the temperature difference between the heating object and the fluid around is maximized. As the fluid is heated, it starts to go up, as the flow is driven by buoyancy forces. Therefore, the discharging heat exchanger is supposed to be placed closer to the top of the tank, to make use of most of the high-temperature energy stored in the tank.

Due to temperature stratification, the quality of energy can differ, even for two tanks with the same amount of energy stored. Exergy is the parameter that quantifies the thermodynamic quality of energy. Research has shown that the exergy content of a tank decreases gradually as the thermocline layer thickness increases [11,12]. That's why it is important to design the thermocline storage tank in a way that reduces the thermocline layer thickness.

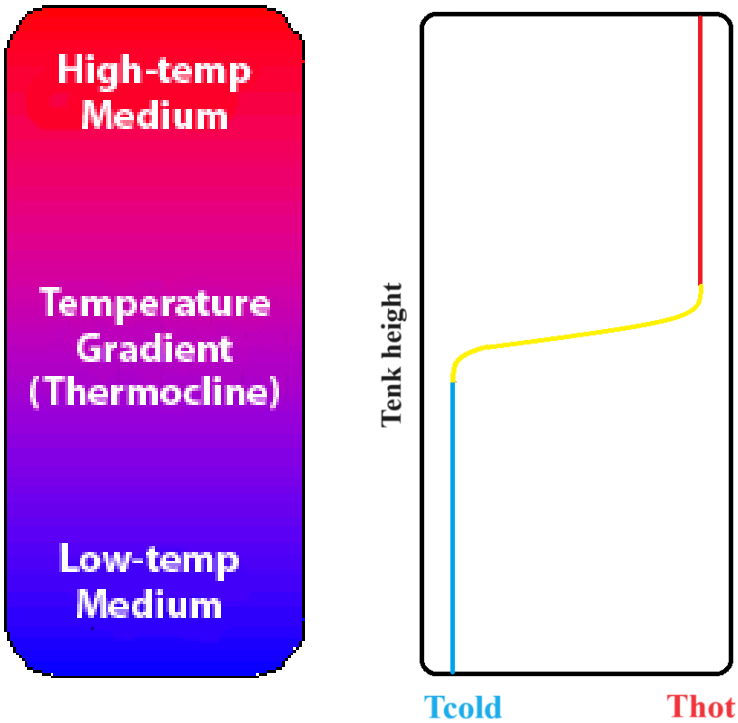

FIGURE 1.14: TEMPERATURE GRADIENT IN THERMOCLINE ENERGY STORAGE

1.5 Project overview

The thermocline energy storage prototype has been developed by ENEA within ORC-PLUS (Organic Rankine Cycle – Prototype Link to Unit Storage) project, in the frame of Horizon2020 [13]. This storage unit is charged from the linear Fresnel concentrated solar field and discharged by ORC power block (figure 1.15). It consists of two heat exchangers, and they are connected by the channel that directs the motion of the HSM during charging and discharging processes. In Figure 1.15, the operating temperatures of both cycles are indicated. Thermocline storage is filled with molten salt (HITEC XL), and thermal oil is used as heat transfer fluid.

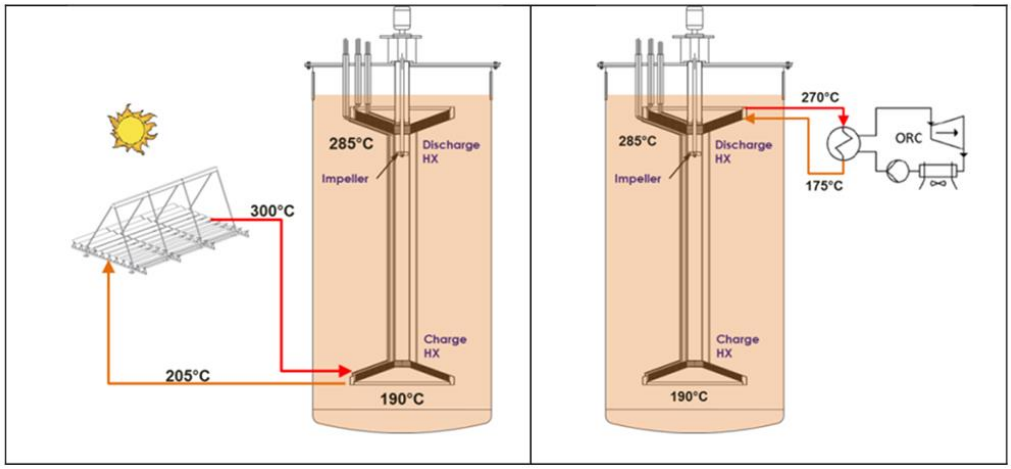

FIGURE 1.15: COUPLING OF TES WITH CSP FIELD AND ORC UNIT [15]

In the process of the design of TES for this application, first, the *Matlab* model of the temperature stratification of the storage unit during charging and discharging processes was developed, for both natural and forced convection flows around heat exchangers [14]. The model showed results in favor of forced convection flows, with the possibility of mass flow rate control, as it provides better thermal stratification compared to natural convection flows. That is why the prototype includes an impeller that is supposed to control the mass flow rate of the salt inside the channel.

Later, TES was analyzed on a system level, to simulate different operating conditions of power production by ORC power block, using thermal energy of the developed TES model [15]. After the construction of the developed TES model, an experimental campaign was carried out with measurements of the temperature stratification of the salt in both charging and discharging processes [16]. Additionally, a CFD model of the thermocline storage was developed, and was validated with results from the temperature measurements of the experimental campaign [17].

The following step of the project is adding photovoltaic field to the existing CSP system. Regarding this step, the new thermocline model has been developed with additional charging heat exchanger, also using thermal oil as HTF. The thermal oil is heated by an electric heater connected to the PV field, outside of the TES (research yet to be published). The new heat exchanger also comes with a metal casing and its channel for the direction of the flow from bottom to the top of the tank (Figure 1.16). The charging-channel-discharging construction that was previously developed is now moved from the tank axis, and the new construction for charging from PV field is added in parallel. This represents the model for indirect heating of the TES from PV field, because the electric heater first heats the HTF outside of the TES, and then the HTF heats the HSM of the TES.

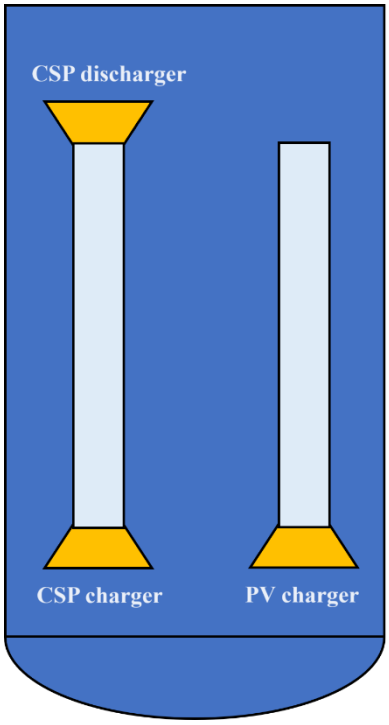

FIGURE 1.16: MODEL OF A TES WITH INDIRECT HEATING FROM PV FIELD

Research of this thesis aimed to model an electric heater immersed in thermocline TES, for the direct heating from photovoltaic field. With direct heating, the number of elements of the system is reduced, as there is no need for additional thermal oil loop for heat transfer. Different configurations of the immersed heater are analyzed, and their geometry is modeled based on parametric studies (paragraph 3).

2. Theory

This paragraph describes the basic concepts of Computational Fluid Dynamics (CFD) and its application to heat transfer problems. Additionally, basics of natural convection are explained, since this thesis models fluid flows driven by buoyancy forces. It includes the literature review of phenomena related to this research.

2.1 Computational thermal Fluid Dynamics

Thermal Fluid Dynamics studies the behavior of fluids considering temperature changes. This behavior is described with a set of non-linear partial differential equations (PDE), which include Navier-Stokes equations, and energy equation. For incompressible flows, the set of PDEs is [18]:

$$\mathrm{div}\,\vec{v} = 0 \tag{2.1}$$

$$\frac{\partial u_i}{\partial t} + \mathrm{div}(u_i\vec{v}) = \mathrm{div}(\nu\,\mathrm{grad}u_i) - \frac{1}{\rho}\mathrm{div}(p\overrightarrow{e_i}) + b_i \tag{2.2}$$

$$\frac{\partial(\rho u_i \mathrm{T})}{\partial x_i} = \frac{\partial}{\partial x_i}\left(\Gamma\frac{\partial \mathrm{T}}{\partial x_i}\right) + q \tag{2.3}$$

Equation 2.1 represents the continuity equation for incompressible flows, where density of the fluid is not a function of pressure.

Equation 2.2 is a momentum equation. It is written in the general form for the i^{th} dimension (in the Cartesian coordinate system, it would be written as a set of equations for each direction $i\epsilon\{x, y, z\}$). First term in the equation $\frac{\partial u_i}{\partial t}$ represents the partial derivative of the velocity component in time. It describes the transient change of the velocity in i^{th} dimension. For steady state solutions, this term is equal to zero. Terms $\mathrm{div}(u_i\vec{v})$ and $\mathrm{div}(\nu\,\mathrm{grad}u_i)$ describe fluid flow caused by advection and diffusion, respectively, where ν is kinematic viscosity of the

fluid. The advective term brings the non-linearity to the equation because it includes the squared velocity component. Term $\frac{1}{\rho}\mathrm{div}(p\vec{e}_i)$ is the driver of the motion of the fluid caused by pressure difference. The direction of the fluid motion is from higher to lower pressure point, which is why the term comes with a negative sign. Considering density not depending on the pressure change in incompressible flows, it can be excluded from the divergence. The last term b_i stands for external drivers of the fluid along the i^{th} direction. It represents the driving force per mass unit $\frac{F_i}{\rho}$ and it is usually used to include gravity force contribution to the fluid motion for models where its contribution is not neglected.

Equation 2.3 is the energy equation. This equation is also written in general form, and it represents the set of equations that describe the rate of change of temperature along each *i* dimension. Since velocity field is completely described by Navier-Stokes equations (4 unknowns including 3 velocity components and pressure, solved in 4 equations), the energy equation considers velocity as a known variable, and determines its contribution to the temperature distribution. In problems where temperature field is the main driver of the fluid motion, we have velocity-temperature coupling, and all equations (2.1-2.3) are solved simultaneously. Terms $\frac{\partial(\rho u_i \mathrm{T})}{\partial x_i}$ and $\frac{\partial}{\partial x_i}\left(\Gamma\frac{\partial \mathrm{T}}{\partial x_i}\right)$ represent the rate of heat addition to the fluid due to advection and diffusion (conduction), respectively, where Γ is thermal conductivity of the fluid. Density of the fluid ρ and thermal conductivity Γ are always functions of temperature, and therefore, cannot be excluded from the partial derivatives.

In general, the previously mentioned set of non-linear equations cannot be solved analytically. Therefore, numerical models are developed to approximate the fluid motion and heat transfer with sufficient accuracy, to highlight the behavior of interest for the specific analysis. These models can be defined for laminar or turbulent flows, and the parameter that determines which of the two types is more suitable is usually Reynolds number (Re), a dimensionless parameter that represents the ratio of inertial to viscous forces (equation 2.4).

$$Re = \frac{uL}{\nu} \tag{2.4}$$

In equation 2.4, *L* is characteristic length that depends on the analyzed geometry. In laminar flows viscous forces are dominant, therefore, they are associated with lower Reynolds number, and the flow is characterized by parallel streamlines. Opposed to that, in turbulent flows inertial forces are dominant, and that is why the non-linearity of advective term in PDEs is more significant than with laminar flows. Turbulence brings a chaotic and random motion of the fluid, with creation of vortices (eddies). Figure 2.1 shows the graphical representation of the two flows.

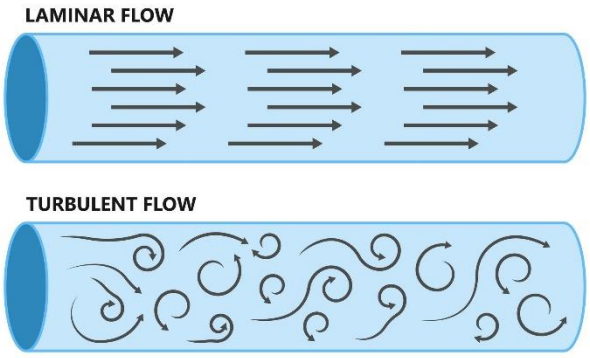

FIGURE 2.1: LAMINAR AND TURBULENT FLOWS THROUGH A PIPE

Highly fluctuating velocity components of turbulent flow bring additional unknowns in the non-linear term that includes squared velocity, and these unknowns are called Reynolds stresses. The Reynolds-averaged Navier-Stokes (RANS) equations define turbulent flows, and contain terms caused by six additional Reynolds stresses - three normal and three shear stresses. To close the system of equations, different RANS turbulence models have been developed. Table 2.1 shows some of the most used RANS turbulence models with highlighted strengths and weaknesses.

Table 2.1: RANS turbulence models

Model name	No. of added equations	Advantages	Disadvantages
Mixing length	0	well established and easy to implement, computationally cheap	incapable of describing separation of recirculation flows
Standard $k-\varepsilon$	2	good at describing fully turbulent flows, validated for many industrially relevant flows	uses predefined wall functions to describe the behavior of the fluid near walls, which is not accurate enough for lower Reynolds number flows
Wilcox $k-\omega$	2	good at describing near-wall flows at lower Reynolds numbers	description of free stream flows can depend significantly on assumed values, and give non satisfactory results
SST $k-\omega$	2	involves switching between equations from both Standard $k-\varepsilon$ and Wilcox $k-\omega$ models depending on the proximity of the walls,	in some cases, like modelling of stagnation regions, and regions with strong accelerations, it

		thus combining the advantages of both models	produces too large turbulence levels
Reynolds stress	7	very accurate calculation of all unknowns, leading to good descriptions of many, but not all flows	very large computational cost due to seven additional equations, and it's not as widely validated as other RANS models

The RANS models are focused on computing macroscopic effects of turbulence, opposed to calculating the real velocity field that would include simulation of all eddies. Other models like Large Eddy Simulation (LES) or Direct Numerical Solution (DNS) provide calculations with higher accuracy, but at an excessive computational cost. Therefore, these models are useful for validation of other turbulence models but are too computationally expensive for engineering applications.

2.2 Natural convection

When the fluid is heated, it expands, and its density reduces. When the heating is localized in one part of the fluid domain, it creates a non-uniform temperature distribution, and the fluid around the heating objects becomes hotter than the surrounding fluid. The fluid at a higher temperature becomes lighter than the fluid at lower temperature, since its density is reduced, and in the steady gravitational field it starts moving up, in the opposite direction of the gravity forces. The force that causes the motion of the fluid due to the density differences is called *buoyancy force*. *Natural convection* refers to heat transfer where the fluid motion occurs spontaneously due to buoyancy forces. Since the density is usually a non-linear function of temperature, Navier-Stokes equations for describing flows driven by natural convection become complex. *Boussinesq approximation* refers to a method of simplifying this set of equations, for fluid flows where variation of density in the range of operating temperatures is relatively small compared to initial or reference density [19]. The first approximation is linearization of density function:

$$\rho(T) \cong \rho_0[1 - \beta_T(T - T_0)] \tag{2.5}$$

In equation 2.5, ρ_0 stands for density at a reference temperature (usually either initial, or mean operating temperature), and β_T is thermal expansion coefficient. The second approximation is that density is regarded as a function of temperature only in buoyancy force term in the equations, and in all other terms it is assumed constant (at reference temperature). This way, the effect of motion caused by temperature differences is captured, while at the same

time simplifying the rest of the equations. Equations 2.6 and 2.7 represent buoyancy force, and adaptation of momentum equation with Boussinesq approximation, respectively.

$$\overrightarrow{F_b} = \rho(T) g \overrightarrow{e_g} \tag{2.6}$$

$$\frac{\partial u_i}{\partial t} + \mathrm{div}(u_i \vec{v}) = \mathrm{div}(\nu\, \mathrm{grad} u_i) - \frac{1}{\rho_0}\mathrm{div}(p\vec{e}_i) + g[1 - \beta_T(T - T_0)]\overrightarrow{e_g} \tag{2.7}$$

2.2.1 Buoyancy-driven cavity

Buoyancy-driven cavity is the most studied case of natural convection driven fluid flow. It describes the circular motion of the fluid inside the cavity that has isothermal walls on the sides, one with high, and the other with low constant temperature, and adiabatic walls on the top and bottom. As the fluid heats from the hot temperature wall, it starts moving up, due to buoyancy forces, and when it reaches the cold wall, it cools down and begins moving in the direction from top to bottom (Figure 2.2 [20]). This creates a circular flow inside the cavity.

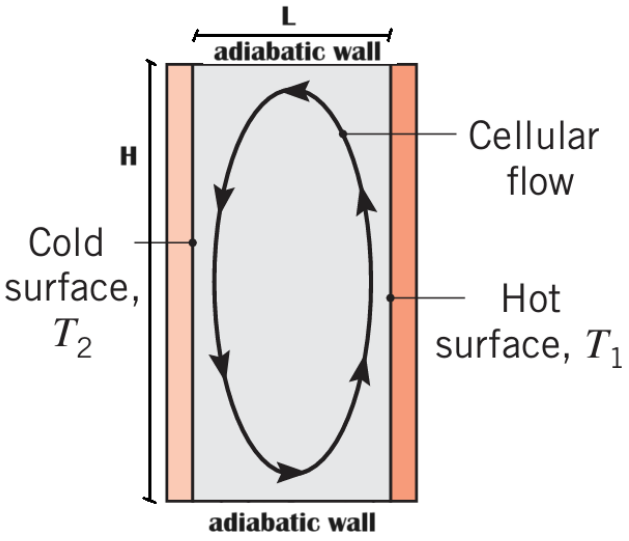

FIGURE 2.2: BUOYANCY-DRIVEN CAVITY

Rayleigh number (Ra) is a parameter useful for determining if the flow driven by natural convection has laminar or turbulent nature. It is calculated as the ratio of buoyant and viscous forces. Equation 2.8 is the formula for calculating Rayleigh number for buoyancy driven cavity.

$$Ra = \frac{g\beta_T \Delta T L^3}{\alpha \nu} \tag{2.8}$$

One way of validation of numerical models for thermal fluid dynamics is comparison of the results with well-established benchmark cases. For natural convection flows, usually the behavior is compared with Nusselt number (Nu) relations with Rayleigh number. Nusselt number represents the ratio of heat transfers by convection and conduction. Equation 2.9 shows the formula for its calculation, where $\bar{h}$ is the average heat transfer coefficient along the heating surface, l is the characteristic length, and k is thermal conductivity of fluid. Characteristic length varies from case to case, and for buoyancy-driven cavity it can be defined as either height (Nu_H) or length (Nu_L) of the cavity.

$$\overline{Nu} = \frac{\bar{h} l}{k} \tag{2.9}$$

Equations 2.10 [20] and 2.11 [21] represent different relations from literature for Nusselt number dependency on Rayleigh and Prandtl ($Pr = \frac{\mu c_p}{k}$, where c_p is the specific heat and μ dynamic viscosity of the fluid) numbers.

$$\overline{Nu} = 0.34 \left(\frac{H}{L}\right)^{\frac{1}{9}} Ra^{\frac{2}{9}} \tag{2.10}$$

$$\overline{Nu} = 0.22\left(\frac{Pr}{0.2 + Pr} Ra\right)^{0.28} \left(\frac{H}{L}\right)^{-\frac{1}{4}} \tag{2.11}$$

2.2.2 Natural convection around horizontal cylinder

When fluid is heated by a horizontal cylinder, there is a formation of boundary layers and plumes due to natural convection, as shown in Figure 2.3 [20]. The figure also shows the distribution of local Nusselt number along the cylinder walls. The maximum is achieved at the bottom of the cylinder. Natural convection around coil cylinders can also be compared with relations for horizontal cylinders because the external heat transfer does not depend much on the curvature of the cylinder [22].

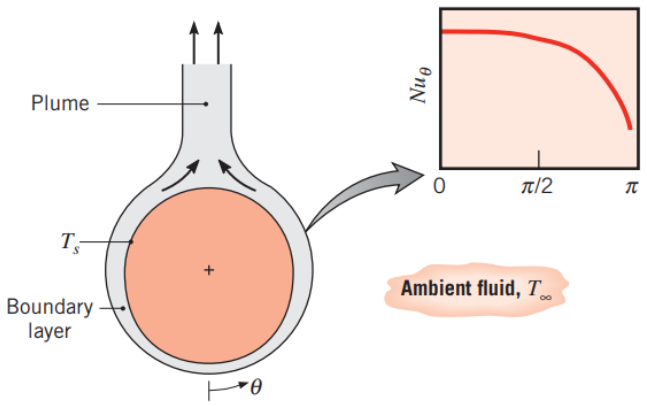

FIGURE 2.3: HORIZONTAL CYLINDER HEAT TRANSFER CHARACTERISTICS

Many relations for Nusselt number dependency on Rayleigh number were analyzed, and some of them are Churchill & Chu (2.13), Lu (2.14), Tsubouchi (2.15) and Fand (2.16) [20,22,23]. Formula for Rayleigh number calculation is given in Equation 2.12. Characteristic length for Nu calculation in this case is the diameter of the cylinder (d). Figure 2.4 shows the graphical representation of these relations for a wide range of Rayleigh numbers.

$$Ra = \frac{g\beta_T(\overline{T_{wall}} - T_\infty)d^3}{\alpha\nu} \tag{2.12}$$

$$\overline{Nu} = \left\{ 0.6 + \frac{0.387\ Ra^{\frac{1}{6}}}{\left[1+\left(\frac{0.559}{Pr}\right)^{\frac{9}{16}}\right]^{\frac{8}{27}}} \right\}^2 \tag{2.13}$$

$$\overline{Nu} = 0.63357 + 0.44681\ Ra^{0.2566} \tag{2.14}$$

$$\overline{Nu} = 0.36 + 0.48\ Ra^{0.125} + 0.52\ Ra^{0.25} \tag{2.15}$$

$$\overline{Nu} = 0.4\ Pr^{0.0432}\ Ra^{0.25} + 0.503\ \ Pr^{0.0334} Ra^{0.0816} + \frac{0.958\ Ge^{0.122}}{Pr^{0.06}\ Ra^{0.0511}} \tag{2.16}$$

In equation 2.16, $Ge = \frac{g\beta_T d}{c_p}$ stands for Gebhart number. With adding Pr and Ge to the correlation, Fand also considers the effect of viscosity dissipation on heat transfer.

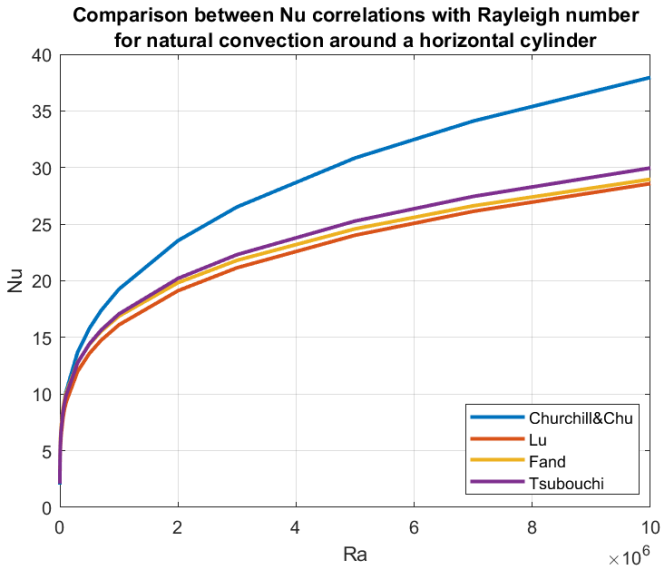

FIGURE.2.4: NUSSELT NUMBER CORRELATIONS FOR HORIZONTAL CYLINDER HEATING

2.2.3 Vertical array of a set of cylinders

Lu et al. [22] examined the impact of temperature and velocity distributions of the fluid surrounding a horizontal cylinder on the heat transfer properties of nearby cylinders aligned vertically.

First, for a set of two vertically aligned cylinders, it has been observed that both local and average Nusselt number of the lower cylinder remain unaffected by the presence of the upper cylinder. Therefore, relations from paragraph 2.2.1 can be applied for the lower cylinder. The heat transfer of the downstream cylinder is highly influenced by the spacing (S) between the two cylinders, normalized by the cylinder diameter ($\frac{S}{d}$). Equation 2.17 shows the dependency of the Nusselt number of the downstream cylinder on the spacing and Rayleigh number. Graphical representation of this equation for different Rayleigh numbers is given in Figure 2.5. Dotted lines on the graph represent the Nusselt number of a single cylinder. It is evident that for each Rayleigh number, there is a specific spacing between cylinders for which the Nusselt number of the upper cylinder equals that of the lower cylinder (critical spacing). Spacings lower than this one result in reduced Nusselt number due to the temperatures of the boundary layers created around the lower cylinder that disturb the heat transfer of the upper one. However, if the spacing exceeds the critical one, the velocity field of the lower cylinder's plume enhances the heat transfer of the upper cylinder (Figure 2.6). As the Rayleigh number increases, the critical spacing between the cylinders decreases.

$$Nu = 0.24414 + 0.3659\left(\frac{S}{d}\right)^{0.2334} Ra^{0.2539} \tag{2.17}$$

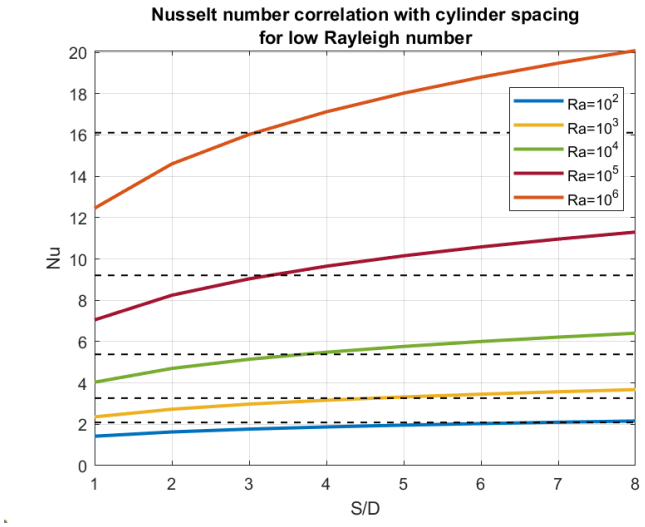

FIGURE 2.5: DOWNSTREAM CYLINDER NUSSELT NUMBER DEPENDING ON CYLINDER SPACING

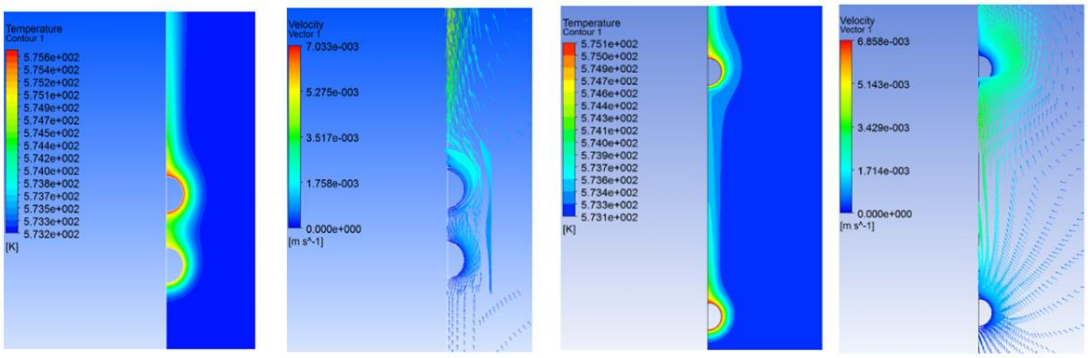

A) *B)*

FIGURE 2.6: TEMPERATURE AND VELOCITY FIELDS FOR TWO CYLINDERS AT A) $\frac{S}{d} = 2$ *B)* $\frac{S}{d} = 9$ *[22]*

Figure 2.7 shows the average Nusselt number of vertically aligned sets with different numbers of cylinders. It demonstrates that for smaller spacings, the average Nusselt number has a decreasing trend as the number of cylinders increases, whereas for larger spacings, the trend is upward. The trends are also significantly affected by the Rayleigh number.

Given that the previously mentioned conclusions are based on simulations of flows at lower Rayleigh number and limited to a single row of cylinders, they can serve as a reference point in the design of the heater pattern. However, the design should be adapted to the specific application accordingly.

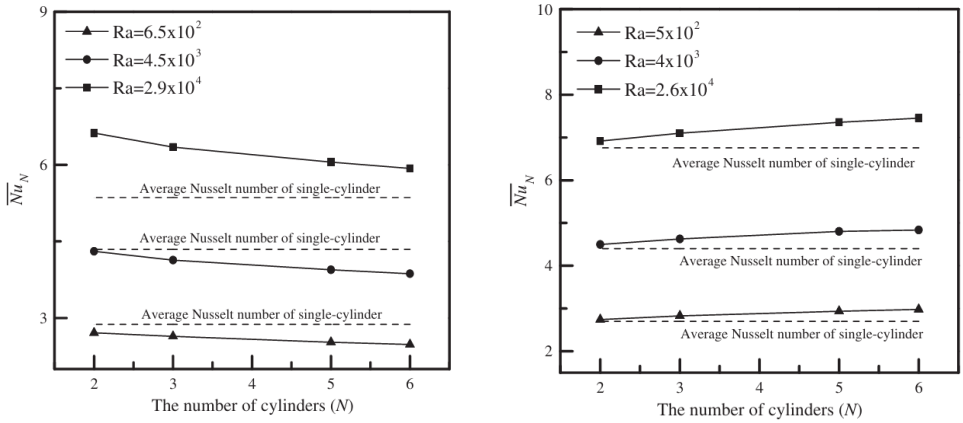

A) *B)*

FIGURE 2.7: AVERAGE NUSSELT NUMBER OF A CYLINDER SET AT A) $\frac{S}{d} = 5$ *B)* $\frac{S}{d} = 10$ *[22]*

3. Methodology

In this paragraph the process of developing the final CFD model of the thermocline with CSP charging and discharging heat exchangers, as well as added electric heater, is explained. First, to test the accuracy of the physics in the numerical models, benchmark cases were simulated. Then, a detailed description of the developed numerical model is presented, including discussion of the domain, boundary conditions, mesh generation and time discretization. Finally, the process of modelling the geometry of the electric heater, for two different heater configurations, is explained through detailed parametric studies.

3.1 Benchmark cases

Considering that the final model simulates a fluid flow driven by natural convection, a well-established benchmark of buoyancy-driven cavity was simulated, to test the properties of molten salt. Additionally, since the model deals with immersed cylindric heating elements, the accuracy of heat transfer characteristics for natural convection around horizontal cylinder was validated. Results from both benchmark cases were compared with different relations from literature.

3.1.1 Numerical modelling of buoyancy-driven cavity

Buoyancy-driven cavity with molten salt was simulated for the height to length of the cavity ratio of $\frac{H}{L} = 2$, and temperature difference between hot and cold wall of $\Delta T = 100℃$. Compared with relations 2.10 and 2.11, the error of simulated average Nusselt number remained below 8%.

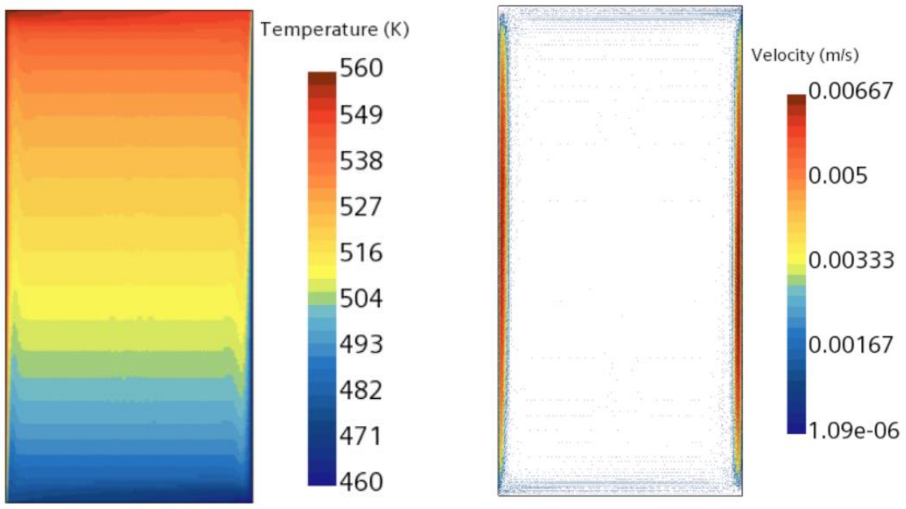

FIGURE 3.1: BUOYANCY-DRIVEN CAVITY TEMPERATURE AND VELOCITY FIELDS

3.1.2 Numerical modelling of natural convection around horizontal cylinder

For the modelling of natural convection around horizontal cylinder, relations by Churchill & Chu, Lu, Fand and Tsubouchi that correlate Nusselt number with Rayleigh number were compared with the results (equations 2.13-2.16). The best fit of the results was achieved with Fand relation, which was also experimentally approved for natural convection of molten salt around fine wire [23]. The error of average Nusselt number retrieved from the simulation with respect to the Fand relation remained below 4%, and of average wall temperature of the cylinder below 3%. Based on the usual practice of numerical modelling that considers errors of calculation of average Nusselt number below 20% acceptable, these simulation outcomes show satisfactory performance.

Figure 3.2 shows the temperature field around the horizontal cylinder. Boundary layers around the wire, and plume formation are clearly indicated, as expected from the literature. These results were achieved with the mesh that consists of 5 prism layers around the cylinder, and mesh refinement around the wire, as well as along the direction of fluid motion (Figure 3.3). This mesh was used as a reference for the mesh generation of the main model (paragraph 3.2.5).

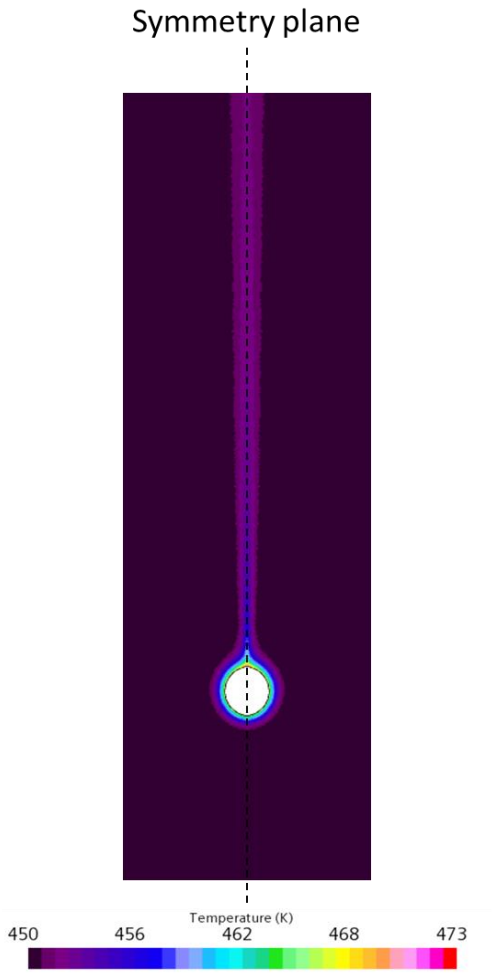

FIGURE 3.2: TEMPERATURE FIELD AROUND HORIZONTAL CYLINDER

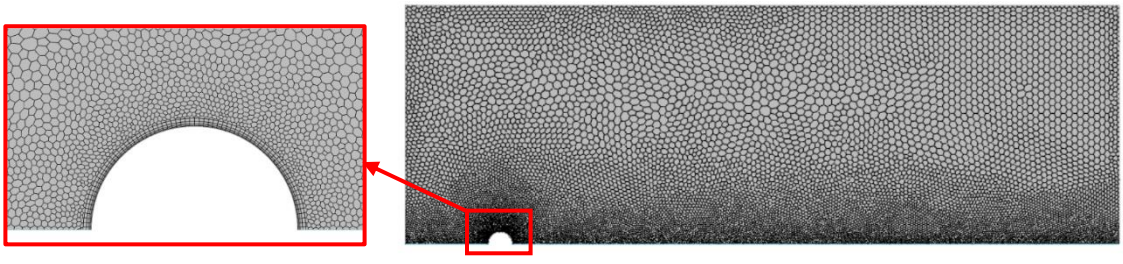

FIGURE 3.3: THE MESH OF HORIZONTAL CYLINDER BENCHMARK MODEL

3.2 Development of the thermocline model with CSP heat exchangers and electric heater

For the design of the electric heater, two different configurations are proposed, and they are modelled based on the parametric study results presented in paragraph 3.3. The principles of both configurations are explained in paragraph 3.2.1. Based on the nature of the geometries of these configurations, the CFD model is developed, and its characteristics are explained through the description of computational domain, physics models, boundary, and initial conditions. The threshold between the computational time and computational accuracy of the simulations is found with the help of grid and timestep independence studies.

3.2.1 Analysis of different electric heater configurations

Conical coil electric heater in series with CSP charger

One of the configurations proposed for the model of the immersed electric heater for this application is electric resistances placed in the shape of conical serpentine, positioned underneath the existing CSP charger. This model of the heater comes with a metal enclosure around the wires, as well as inlet and outlet channels, to direct the motion of the fluid caused by natural convection (Figure 3.4). Driven by natural convection, cold salt enters the heater from the bottom of the tank, through the inlet channel. They then get heated from the electric resistances and exit the heater through the outlet channel. The outlet channel of the electric heater construction has a smaller diameter than the existing channel for CSP heat exchangers, so that the salt can move from the heater channel to the main channel of the TES, and not disturb the operation of already installed elements. The mass flow rate of fluid inside the channel is planned to be controlled by the impeller positioned at the top of the channel [14]. The fact that both chargers can share the same channel that directs the motion of heated fluid to the top of the tank allows the simultaneous control of both flows. It also avoids having to add a whole new channel for the electric heater.

The cone is inclined at an angle of 20 degrees, to align with the existing CSP charger. The arrangement of electric resistances is chosen based on the parametric study explained in paragraph 3.3.

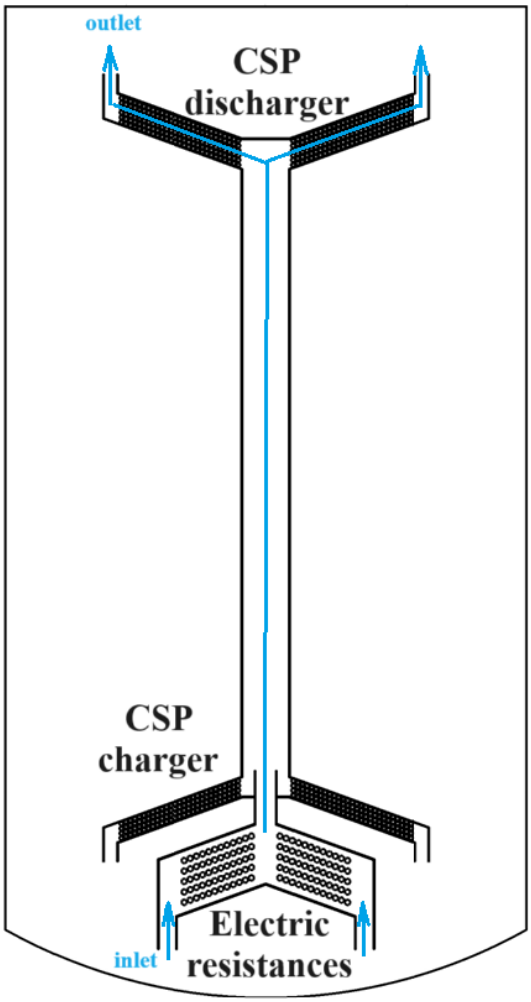

FIGURE 3.4:MODEL OF THE THERMOCLINE WITH CONICAL COIL ELECTRIC HEATER

Electric heater with an annular baffle

This heater model consists of a set of electric resistances loops placed along the lateral walls of the storage tank (Figure 3.5). The function of the annular baffle is to direct the charging flow to the top, while providing more effective heat transfer and faster charging. Both annular baffle and channel from previous configuration have a purpose to provide charging of the tank from the top, and in that way provide better temperature stratification needed for the thermocline TES. The baffle is designed without a shroud region [24]. This configuration is mostly analyzed for discharging heat exchangers, and the presence of the annular baffle has

proved to increase heat transfer characteristics, and effectiveness of the discharge, as well as solar fraction for solar thermal technologies [25, 26].

Having the diameter of the wire loops almost the same as the diameter of the whole tank, since the wires are placed along the lateral walls, means that the total number of loops is decreased. Decreasing the total number of wires increases the heat transfer coefficient [22]. The pressure drop over the heating element decreases, because the fluid faces less obstacles [27]. The fact that fluid flow is unidirectional, unaffected by any tilting of the heater construction, further contributes to the decrease in pressure drop.

The arrangement of the wires for this application was chosen based on the parametric study explained in paragraph 3.3.

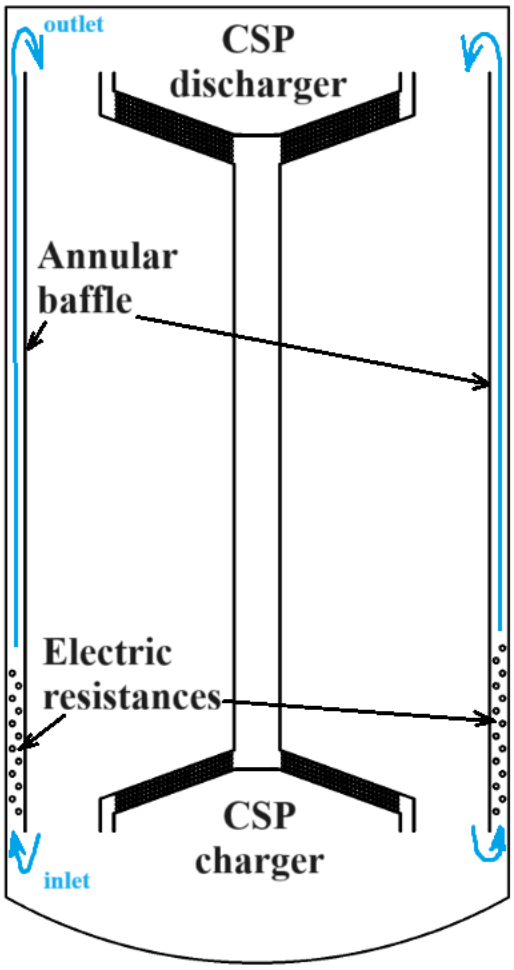

FIGURE 3.5: MODEL OF A THERMOCLINE WITH ELECTRIC HEATER WITH AN ANNULAR BAFFLE

3.2.2 Computational domain

The geometry of the thermocline TES prototype designed by ENEA for the purpose of ORC-PLUS project [13] can be approximated as axisymmetric. The main components that affect the temperature distribution of the tank are the shape of the tank, geometry of CSP charger and discharger serpentines with the channel, and thermal load, and they are all axisymmetric. Additionally, as explained in the previous paragraph, both electric heater configurations analyzed in this thesis are axisymmetric. The elements like support structures, connection wires and tubes, and flanges at the top of the tank, are the components that are not axisymmetric, but their contribution to the temperature field of the tank can be neglected, as it was shown through previous research on the project [17]. Therefore, the domain of the numerical model developed for the purpose of analyzing the charging transient of electric heater added to the existing thermocline TES prototype construction is 2D axisymmetric model. Reducing the domain of the thermocline from 3D model to 2D model decreases the computational complexity of the model drastically, while at the same time providing accurate results of the charging process of the storage tank.

Figure 3.6 shows the computational domain of the CFD model analyzed in this thesis, with highlighted boundaries, that are further explained in the following paragraph. The domain consists of a 2D half cross-section of the tank, and it includes the elements that affect the flow and temperature fields of the fluid the most, and they are:

- **Serpentine for charging of the tank from CSP field** – consists of 4 rows of heat exchanger loops, each with 28 tubes.
- **Serpentine for discharging of the tank by ORC system** – consists of 6 rows of heat exchanger loops, each with 28 tubes.
- **Metal casing with the channel** – provides the construction for directing the fluid motion during charging (from the bottom to the top) and discharging (from the top to the bottom) processes.
- **Electric heater for charging of the tank from PV field** – together with the enclosure, or baffle, depending on the configuration. The number and arrangement of the electric wires are based on the parametric studies of both configurations.
- **Walls of the tank** – convection losses from the tank to the environment modelled with boundary conditions (paragraph 3.2.4)

The whole domain is filled with molten salt, and the thermophysical properties of the material can be found in table 3.1. Solid elements of the domain are not simulated but replaced with proper boundary conditions.

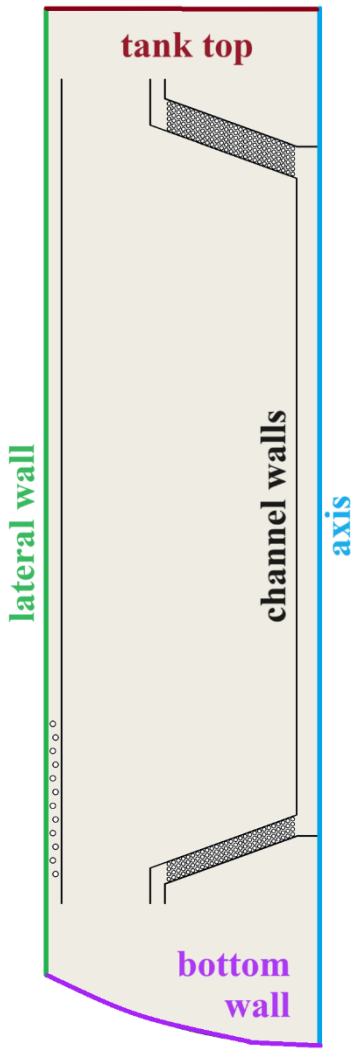

FIGURE 3.6: COMPUTATIONAL DOMAIN WITH INDICATED BOUNDARIES

Table 3.1: Molten salt (HITEC XL) properties [17]

Density $[\frac{kg}{m^3}]$	$\mathbf{2240 - 0.827\ (T[K] - 273.15)}$
Dynamic viscosity $[Pa \cdot s]$	$10^{6.1374}(T[K] - 273.15)^{-3.36406}$
Specific heat $[\frac{J}{kg\ K}]$	$1584 \pm 4.6\%$
Thermal conductivity $[\frac{W}{m\ K}]$	0.519

3.2.3 Physics models

The list of physics models from StarCCM+ used for the simulations in this thesis is shown in Table 3.2, along with the explanation of the choices.

Table 3.2: List of physics models used in simulations

Physics model	Justification of the choice
2D axisymmetric	The geometry of the storage tank allows the simplification of the domain from 3D to 2D axisymmetric model (paragraph 3.2.1).
Implicit unsteady	The results of the simulations are analyzed based on the transient temperature and velocity changes of the fluid during the charging process. Implicit scheme is preferred to explicit because of the unconditional computational stability [18].
Boussinesq approximation	Simplification of the Navier-Stokes and energy equations for the numerical modelling of the fluid flow driven by buoyancy forces is accurately done with Boussinesq approximation for flows where variation of the density in the operating range of temperatures is relatively small compared to the reference density (paragraph 2.2).
Constant density	Software requires Boussinesq approximation coupled with constant density model, and the thermal expansion coefficient, both derived from density equation of the molten salt (table 3.1).
Gravity	Buoyancy forces are driven by gravity.
SST k-ω turbulent model	This turbulence model uses the advantages of both standard $k-\varepsilon$ model, which accurately describes

	free turbulence streams far from the walls, and the $k-\omega$ model, known for the precise calculation of near-wall flows. Achieving this involves switching between equations from both models depending on the proximity of the walls. This approach has proven to be beneficial in numerical modelling of the separation flows [28]. SST $k-\omega$ turbulence model was already used for 2D axisymmetric CFD modelling of this thermocline prototype and was validated with experimental results [17].

3.2.4 Boundary and initial conditions

As indicated in paragraph 3.2.2, solid parts of the storage tank are replaced with boundary conditions. That includes:

- **Electric resistances** – walls with constant heat flux heating
- **CSP charging heat exchanger** – models simulate only charging from electrical heater, therefore heat exchanger tubes are modeled as adiabatic walls
- **CSP discharging heat exchanger** – adiabatic tube walls
- **Channels and metal casings** – adiabatic walls
- **Lateral tank walls** – convection losses to the environment are modeled based on the Churchill & Bernstein correlation for Nusselt number (Nu) dependency on Reynolds (Re) and Prandtl (Pr) numbers [29]:

$$Nu = 0.3 + \frac{0.62Re^{1/2}Pr^{1/3}}{(1+(\frac{0.4}{Pr})^{2/3})^{1/4}}(1+(\frac{Re}{282000})^{5/8})^{4/5} \quad (3.1)$$

- **Bottom tank wall** – convection losses to the environment are modelled based on the correlation for Nu number dependency on Re, Pr, and critical Reynolds number (Re_c) that defines the transition from laminar to turbulent flow [21]:

$$Nu = (0.037Re^{\frac{4}{5}} - 0.037{Re_c}^{4/5} + 0.664{Re_c}^{1/2})Pr^{1/3} \quad (3.2)$$

- **Top of the tank** – convection losses were modelled based on a 3D simulation of salt in contact with air at the top of the tank, considering all elements like connections and flanges, during previous research on ORC-PLUS project [13]

For simulations carrying out the control of mass flow rate of the fluid inside the channel, pressure drop was imposed using *fan interface*. For simulating constant mass flow rate charging, boundary conditions were set as *inlet* and *outlet*, at the channel entrance.

Regarding initial conditions, the simulation considers a uniform temperature distribution among the whole domain of the salt, and atmospheric pressure. The initial temperature of 450K assumes that salt was pre-heated up to the reference temperature of cold salt of the thermocline.

3.2.5 Mesh generation and grid independence study

The mesh characteristics of the model were based on the mesh from benchmark simulation (paragraph 3.1.2) that provided satisfactory results. That involves 5 prism layers around all heating elements, refinement of the mesh along the channels, and slow growth rate of the cells-1.03 (Figure 3.7). These parameters were kept constants for all simulations of grid independence study. The only parameter that was changed was the base of the cell.

For grid independence study, the model was simulated for transient time of 20 minutes, with the timestep of 5 seconds. The number of cells varied from 10 to 125 thousand. Throughout each simulation, temperature readings were taken at 4 specified nodes, illustrated in Figure 3.8. The values of temperatures obtained from the simulation with the most refined mesh (with 125 thousand cells) were considered as the accurate representation of the temperature field inside the tank.

For each temperature node, the computation error was determined as the relative error with the reference temperature of 450K, which is the initial temperature of the salt (3.3).

$$\delta_T = \frac{T_{node}[K] - T_{correct}[K]}{T_{correct}[K] - 450K} \cdot 100\% \tag{3.3}$$

Furthermore, different grids were compared based on the average temperature of the salt. This calculation accounts for the correct computation of energy balance equation. The outcomes of the grid independence study are presented in Figure 3.9, highlighting the highest point error among the 4 calculated temperatures in each simulation, as well as average temperature error. The maximum point error occurred for the temperature of node A in each simulation.

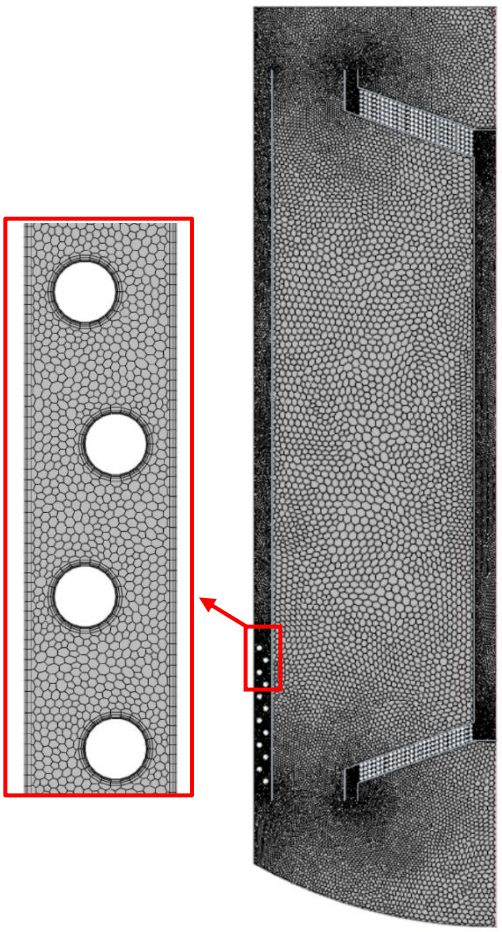

FIGURE 3.7: THE MESH

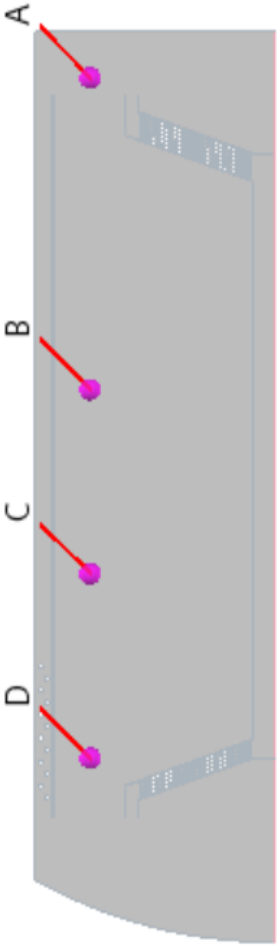

FIGURE 3.8: TEMPERATURE MEASUREMENT NODES

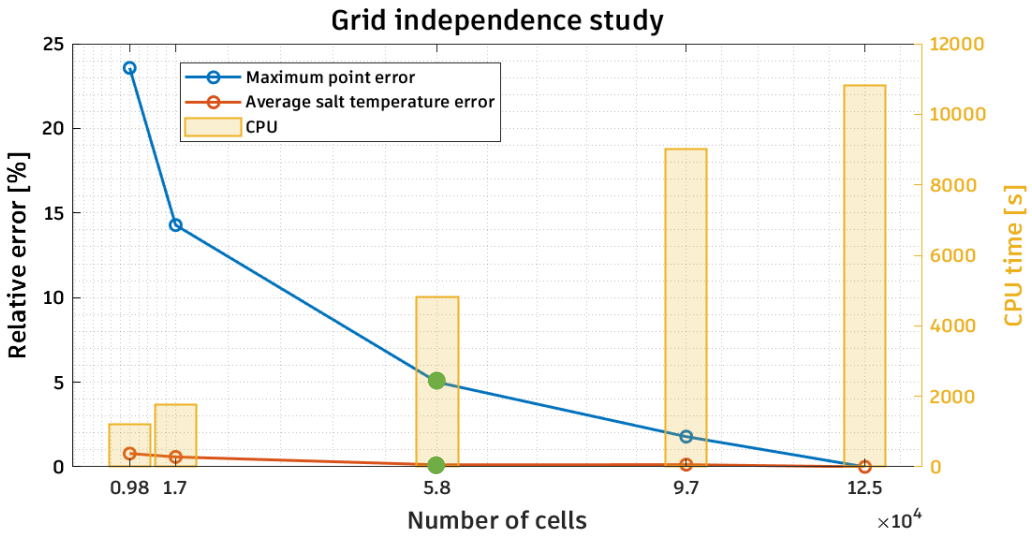

FIGURE 3.9: GRID INDEPENDENCE STUDY

Increasing the number of cells results in the decrease of calculation error, but at the same time the simulation becomes more computationally expensive. Figure 3.9 also shows the total computational time required for each grid. As a balance between accuracy and computational cost, the grid with *5.8 thousand* cells was chosen. The error of temperature field estimation with the chosen grid remains below 5%, and the computational time is reduced by more than 50% compared to the reference grid.

3.2.6 Timestep independence study

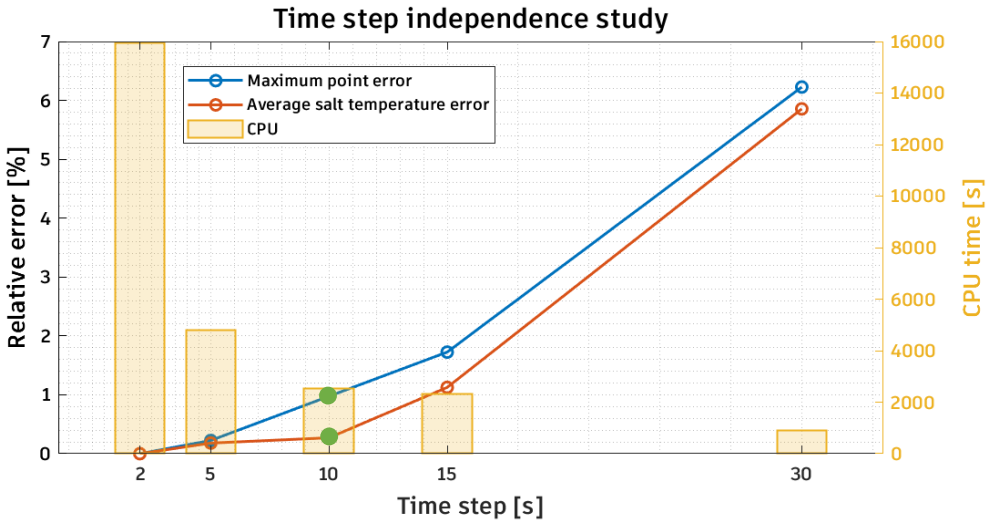

FIGURE 3.10: TIME STEP INDEPENDENCE STUDY

Using the mesh chosen in the previous paragraph, the model was simulated with 5 different timesteps, ranging from 2 to 30 seconds. Taking the results from the simulation with the shortest timestep (2 seconds) as a reference accurate solution, the relative errors of temperature calculations of the same 4 points as in grid independence study, were used for accuracy comparison between simulations. Figure 3.10 shows the trends of maximum point error and average temperature error depending on the timestep, along with the computational cost of each simulation. The timestep of *10 seconds* was chosen, as it provides calculations with the maximum error below 1%, and at the same time drastically reduces the computational time compared to the simulation with the shortest timestep.

3.3 Improvement of the heat transfer characteristics of electric heater

The peak power of photovoltaic field anticipated by ENEA is $190kW$. Since the maximum heat flux that can be achieved by commercial immersion electric heating elements is around $100\frac{kW}{m^2}$ [30], electric heaters for both heater configurations are designed to have a total heating surface close to $1.9m^2$.

For immersed heat exchangers, as well as electric heaters, the objective is to enhance the convective heat transfer to ensure an even temperature profile around the heating elements. This approach avoids the accumulation of localized high-temperature zones caused by diffusion. When the heat transfer is dominated by conduction, the surface temperatures of the heating elements can reach values that are harmful for the fluid composition surrounding them. For molten salt, decomposition occurs at temperatures higher than 600℃ [31]. The aim of the parametric studies explained in the following paragraphs is to maximize the heat transfer coefficient (HTC), which accounts for more effective heat transfer, and consequently lower maximum temperature of the fluid near heating elements.

All models of parametric studies are simulated for 120 seconds of physical time, which is the time long enough for velocity field to form along the channels.

3.3.1 Conical serpentine in series configuration parametric analysis

Considering the maximum diameter of the electric heating wires, and the limited dimensions required for the heater to fit underneath the existing CSP charger (Figure 3.11), the conical serpentine designed for the purpose of this research consists of 60 electric resistances, each with the diameter of 13mm.

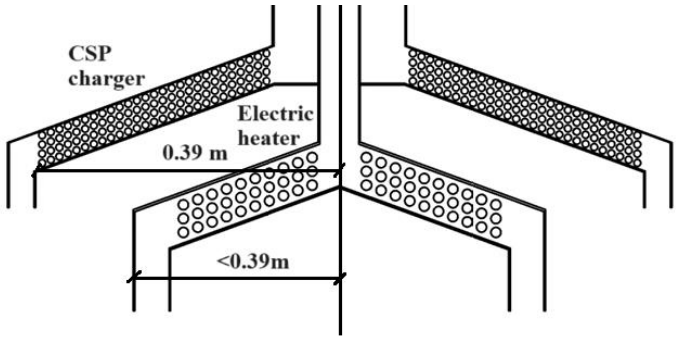

FIGURE 3.11: LIMITS OF THE ELECTRIC HEATER WIDTH

The 60 circular wires are placed in 5 rows of 12 elements. Starting from the geometry where wiring elements are positioned with distances that are 1.25 times bigger than their diameter [32] (Figure 3.12 a)), the longitudinal and transverse pitch were varied with the aim of maximizing the heat transfer coefficient [27], considering previously mentioned dimension limits. All other parameters, such as the length and width of inlet and outlet channels, cone tilt angle, and positions of the wires with respect to the surrounding channel walls are kept constant for better comparison.

Effect of varying the longitudinal pitch

Figure 3.12 shows the models of 3 different geometries analyzed, in terms of variation in longitudinal pitch, indicated in the pictures as S_L. Maximum pitch respecting the limits of the maximum heater width explained previously is $\frac{S_L}{d} = 2$.

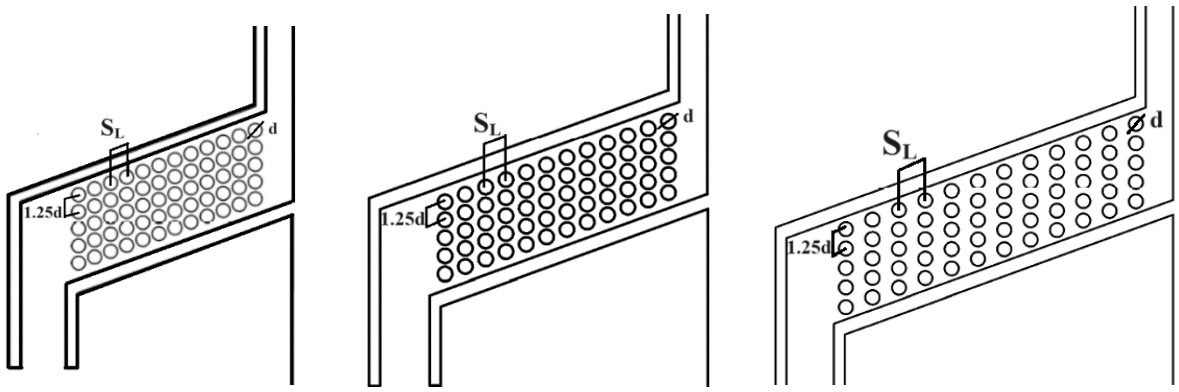

A) *B)* *C)*

FIGURE 3.12: VARIATION OF LONGITUDINAL PITCH MODELS A) $\frac{S_L}{d} = 1.25$ *B)* $\frac{S_L}{d} = 1.5$ *C)* $\frac{S_L}{d} = 2$

Figure 3.13 shows the results of the simulations. It can be noticed that the average heat transfer coefficient does not change drastically as we are increasing the longitudinal pitch. If the longitudinal pitch is increased from $\frac{S_L}{d} = 1.25$ to $\frac{S_L}{d} = 2$, average HTC increases by less than 5%, but the dimensions of the heater increase by more than 35% (indicated in the figure as the cross-section area of the space limited by channel walls). The variation of the longitudinal pitch does not show significant benefits regarding the temperature field of the fluid inside the heater. Therefore, to keep the heating object more compact, for following analysis the first geometry with the longitudinal pitch of $\frac{S_L}{d} = 1.25$ was kept as a reference.

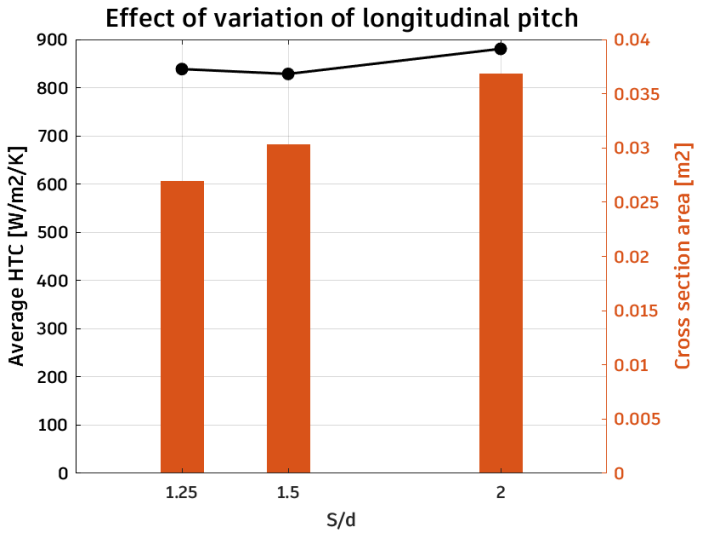

FIGURE 3.13: EFFECT OF LONGITUDINAL PITCH VARIATION ON AVERAGE HTC

Effect of varying the transverse pitch

Models shown in figure 3.14, as well as the model from figure 3.12 a), show the different geometries of the conical serpentine used for a comparative parametric study of determining the effect of variation in transverse pitch to the average heat transfer coefficient.

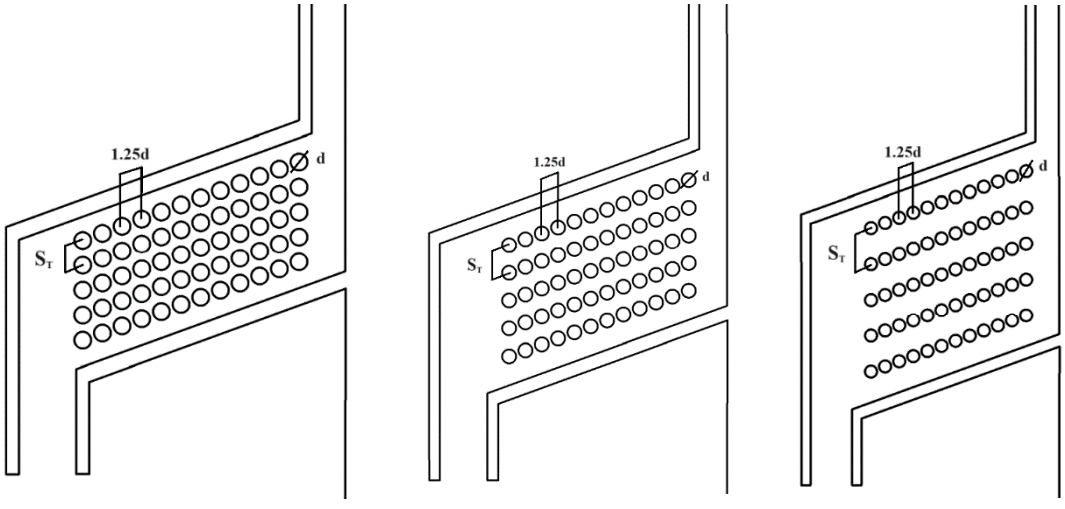

a) *B)* *C)*

FIGURE 3.14: VARIATION OF TRANSVERSE PITCH MODELS A) $\frac{S_T}{d} = 1.5$ *B)* $\frac{S_T}{d} = 2$ *C)* $\frac{S_T}{d} = 3$

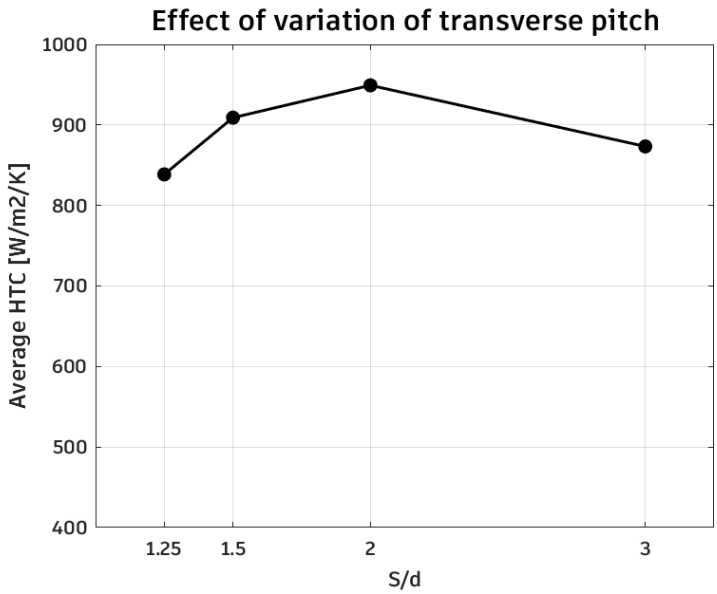

FIGURE 3.15: EFFECT OF TRANSVERSE PITCH VARIATION ON AVERAGE HTC

Figure 3.15 shows the average heat transfer coefficient of 4 different geometries of the heater, each with a different transverse pitch. It can be noticed that the geometry with the transverse pitch of $\frac{S_T}{d} = 2$ maximizes the average HTC.

Compared to the initial reference geometry, the average HTC has increased by 14%. More importantly, this geometry creates the most even flow field around the wires. Streamlines of 3 different geometries are shown in Figure 3.16. With the initial transverse pitch of 1.25, streamlines are formed mostly from the sides of the geometry, skipping a major part of the wires in the middle. Increasing the transverse pitch allows the formation of parallel local flows that enhance the local heat transfer of each wire, accounting for a higher average HTC. Further increase of the transverse pitch (example of $\frac{S_T}{d} = 3$) creates a low resistance path for fluid to pass mainly between first few rows, causing uneven flow field inside the heating object.

Temperature fields around heating elements are a direct consequence of the flow field formed. Figure 3.17 shows the accumulation of high temperature fluid around the wires in the initial reference geometry. It shows that the most uniform temperature distribution is achieved with geometry that maximizes the HTC. As opposed to this, the geometry with transverse pitch of $\frac{S_T}{d} = 3$ creates local high-temperature zones that fluid is unable to reach.

Considering previously mentioned benefits of the geometry with the transverse pitch of $\frac{S_T}{d} = 2$, this geometry is chosen as the design of the conical serpentine electric heater.

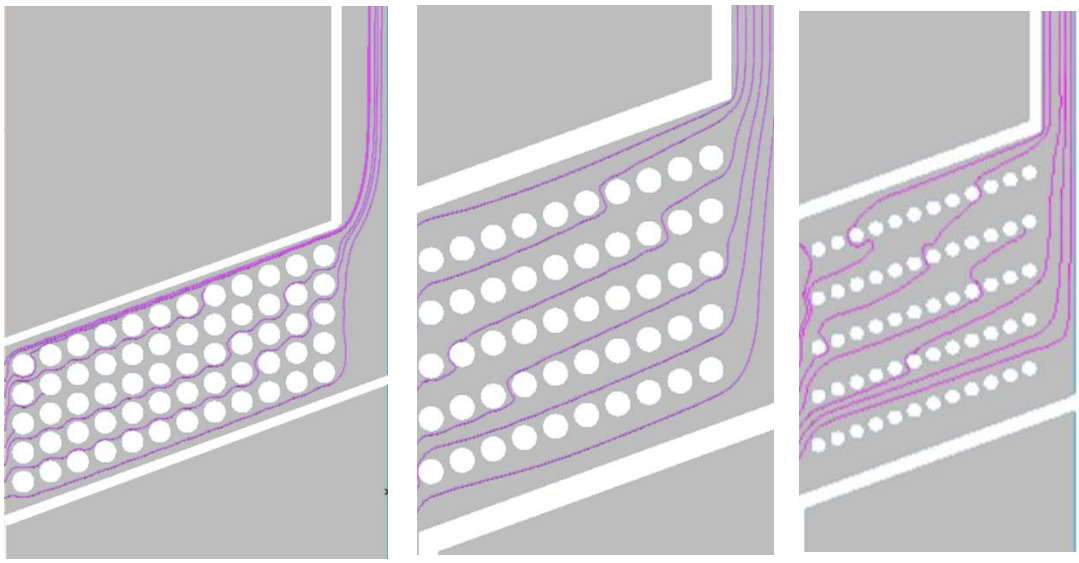

A) B) C)

FIGURE 3.16: STREAMLINES A) $\frac{S_T}{d} = 1.25$ *B)* $\frac{S_T}{d} = 2$ *C)* $\frac{S_T}{d} = 3$

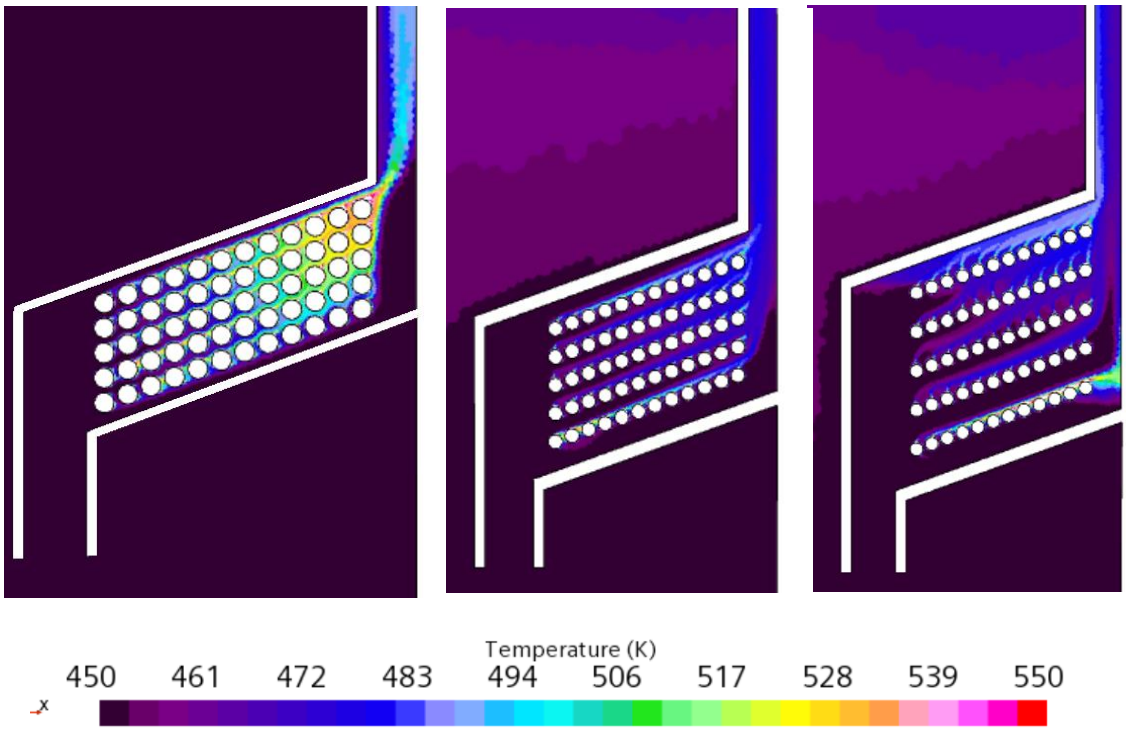

A) B) C)

FIGURE 3.17: TEMPERATURE FIELDS A) $\frac{S_T}{d} = 1.25$ *B)* $\frac{S_T}{d} = 2$ *C)* $\frac{S_T}{d} = 3$

Table 3.3: Effect of transverse pitch variation on maximum salt temperatures

Transverse pitch:	$\frac{S_T}{d} = 1.25$	$\frac{S_T}{d} = 1.5$	$\frac{S_T}{d} = 2$	$\frac{S_T}{d} = 3$
T_{max} [K]	704	697	688	710

Table 3.3 shows the maximum temperatures of the salt achieved by different geometries analyzed. Besides creating the most uniform temperature field, the chosen geometry also provides the least risk of reaching the temperatures of the decomposition of the salt, since it minimizes peak temperature.

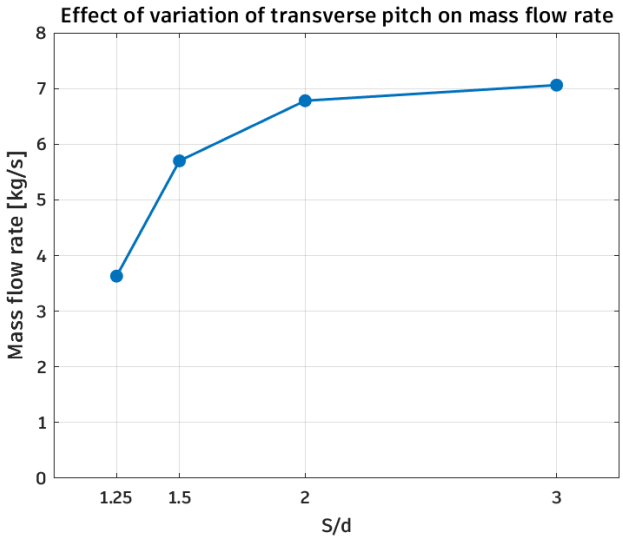

FIGURE 3.18: EFFECT OF TRANSVERSE PITCH VARIATION ON MASS FLOW RATE

Figure 3.18 shows a similar trend of mass flow rate change as the average HTC trend. The exception is the final geometry with the highest transverse pitch. Even though the mass flow rate has slightly increased with respect to the smaller transverse pitch geometry, its average HTC has decreased, because of the uneven flow field inside the heater. Local flow formed between the first and the second row of this geometry moves at the highest velocity but contributes to the heat transfer enhancement only for the wires in the second row, thus making the heat transfer more uneven.

3.3.2 Annular baffle configuration parametric analysis

The total heating surface of $1.9m^2$ corresponds to a geometry of 12 loop wires placed along the lateral walls for the heater configuration with an annular baffle. These 12 wires are arranged to form two parallel sets of 6 wires each. In this configuration, flow is formed from the bottom of the tank and fluids move from bottom to the top, aligning with the direction of natural convection of the fluid around the wires, as there is no tilted geometry like in conical coil heater. Therefore, this configuration allows the application of insights from the literature of vertical arrays of cylinders, explained in paragraph 2.2.3.

In the previous parametric study concerning the modelling of a conical serpentine heater, the reference geometry involved the wires positioned with both longitudinal and transverse pitches of 1.25. The same approach was employed in the parametric study for the annular baffle configuration. Starting from this reference geometry, the longitudinal and transverse pitches were varied with the same aim of maximizing the heat transfer coefficient. All other dimensions like the height of the annular baffle and the distance of the first wire with respect to the bottom of the baffle were kept constant in all geometries for better comparison.

Effect of varying the longitudinal pitch

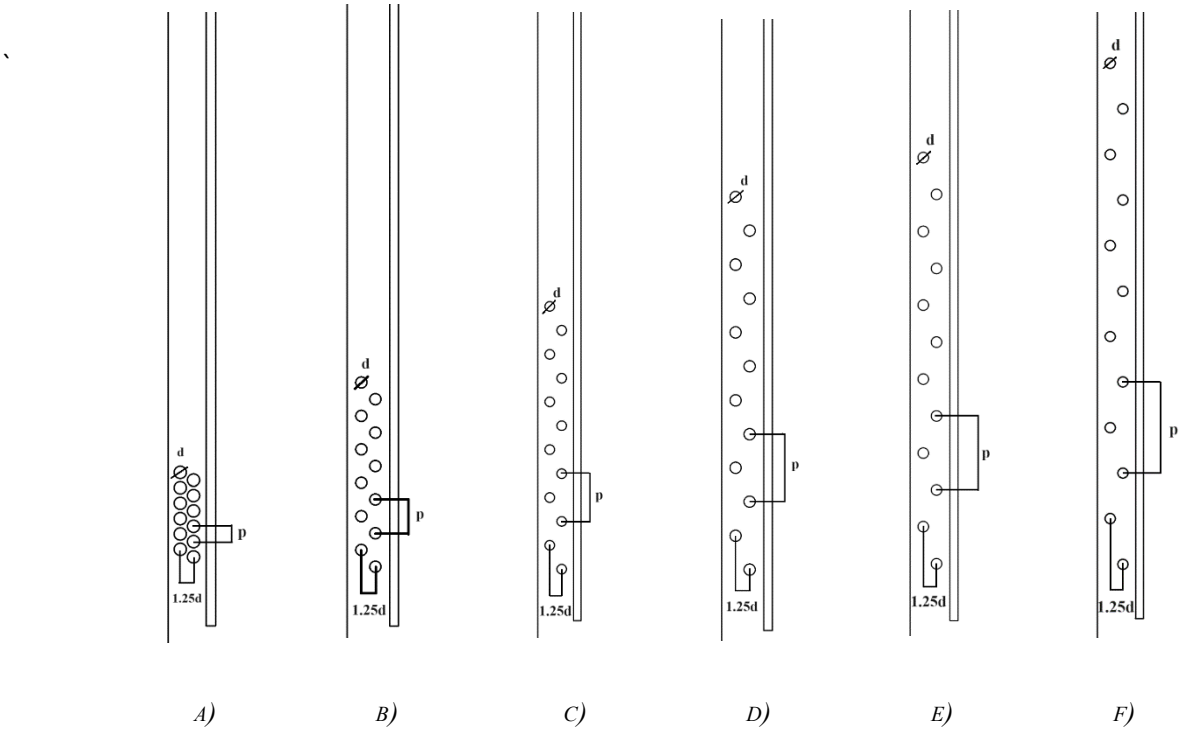

FIGURE 3.19: VARIATION OF LONGITUDINAL PITCH MODELS A) $\frac{S_L}{d} = 1.25$ *B)* $\frac{S_L}{d} = 3$ *C)* $\frac{S_L}{d} = 5$ *D)* $\frac{S_L}{d} = 6$ *E)* $\frac{S_L}{d} = 7$ *F)* $\frac{S_L}{d} = 9$

Figure 3.19 shows the models of different geometry patterns simulated for the analysis of the effect of longitudinal pitch variation on the average HTC. The longitudinal pitch variations were kept in the range from 1.25 to 9. All patterns are staggered, to avoid the increased temperatures of boundary layers around wires disturbing the heat transfer of the adjacent wire (Figure 1.22).

Applying the principles from the theory of vertical set of cylinders, the increase of the longitudinal pitch is expected to enhance the heat transfer. This behavior applied to the heater configuration with annular baffle is shown in figure 3.20.

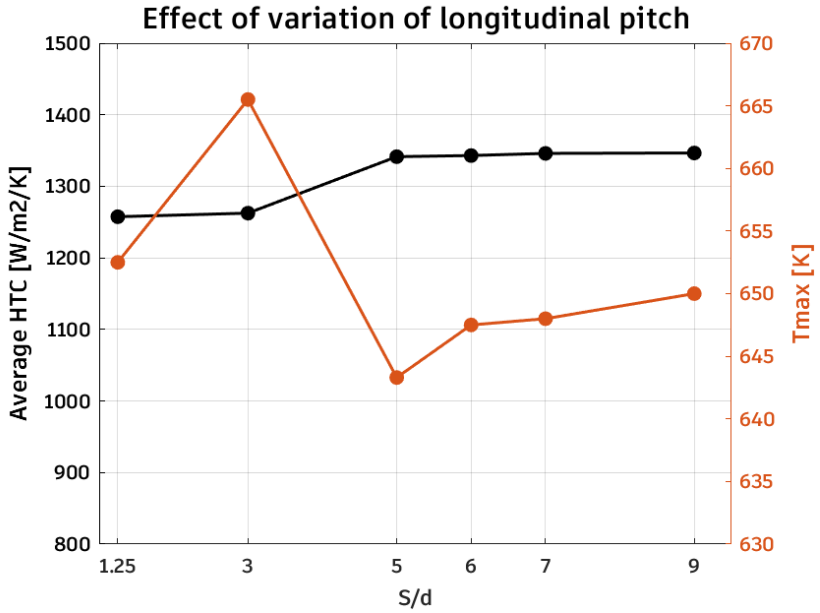

FIGURE 3.20: EFFECT OF LONGITUDINAL PITCH VARIATION ON AVERAGE HTC AND MAXIMUM TEMPERATURE OF THE SALT AROUND THE WIRES

From Figure 2.5 (paragraph 2.2.3) it can be noticed that at longitudinal pitch of around 3, velocity field formed from the bottom cylinder enhances the heat transfer for the upper cylinder. The results from these simulations also show that for longitudinal pitch higher than 3, heat transfer is enhanced. Increasing the longitudinal pitch from 5 to higher values does not contribute to the further enhancement of heat transfer characteristics.

Additionally, Figure 3.20 shows how the variation of the longitudinal pitch affects the maximum temperature of the salt around the wires. It can be noticed that for geometries that have similar average HTC, increased pitch increases the peak temperature of the salt. Figure 3.21 shows the effect of enhanced heat transfer on the temperature fields of salt near heating elements. For further consideration of the heater modelling, the geometry with the longitudinal pitch of $\frac{S_L}{d} = 5$ was chosen as the one that at the same time increases the average heat transfer coefficient and minimizes the peak temperature of the salt.

A)

B)

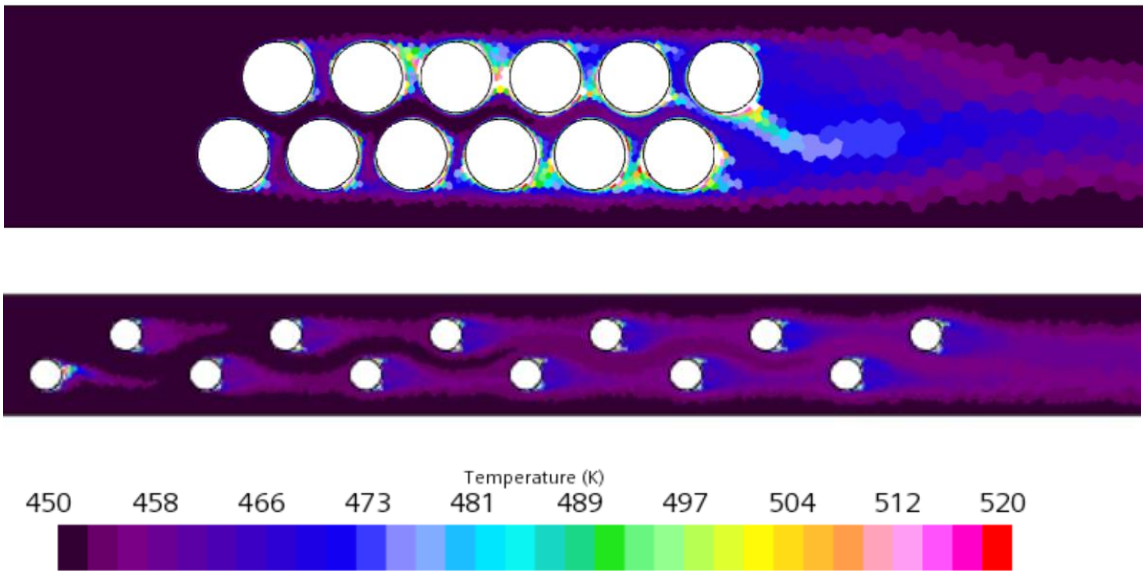

FIGURE 3.21: TEMPERATURE FIELDS OF SALT AROUND WIRES A) $\frac{S_L}{d} = 1.25$ *B)* $\frac{S_L}{d} = 5$

Effect of varying the transverse pitch

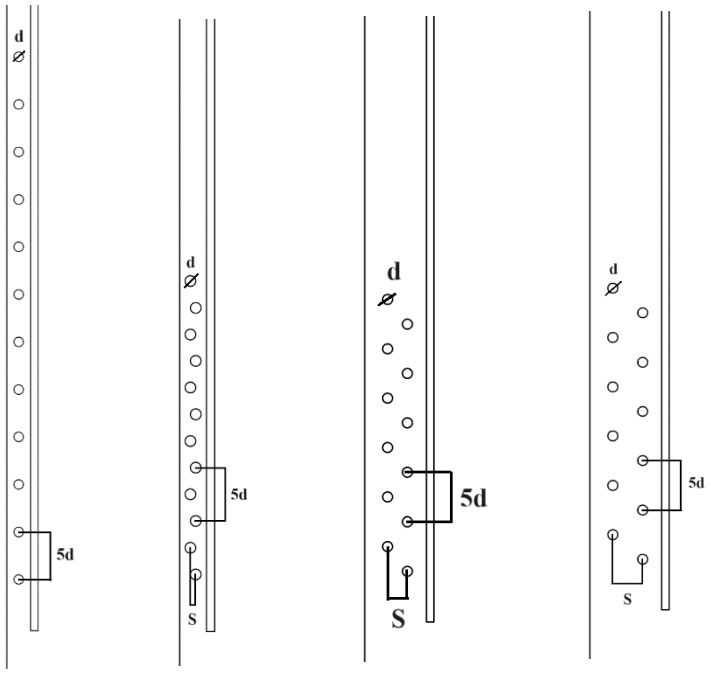

A) *B)* *C)* *D)*

FIGURE 3.22: VARIATION OF TRANSVERSE PITCH MODELS A) $\frac{S_T}{d} = 0$ *B)* $\frac{S_T}{d} = 0.5$ *C)* $\frac{S_T}{d} = 2$ *D)* $\frac{S_T}{d} = 3$

Figure 3.22, along with Figure 3.19 c), shows models of 5 different geometries considered for the analysis of the effect of transverse pitch variation on heat transfer characteristics of the heater. The transverse pitch was changed in the range from 0, which corresponds to the geometry of one set of vertically aligned cylinders, to 3. Along with the variation of the pitch, the width of the baffle changes accordingly. Consequently, as the width of the baffle channel increases, the mass flow rate of the fluid flow also increases (figure 3.23). However, with the increase in mass flow rate, the average HTC does not necessarily increase (figure 3.24).

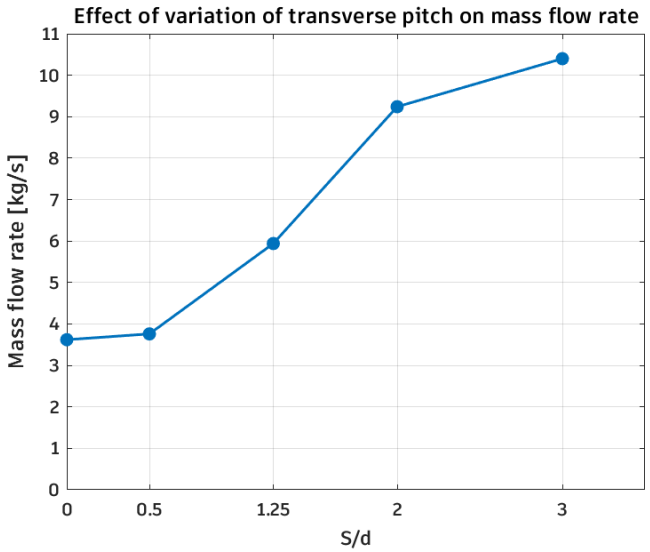

FIGURE 3.23: EFFECT OF TRANSVERSE PITCH VARIATION ON THE MASS FLOW RATE THROUGH THE BAFFLE CHANNEL

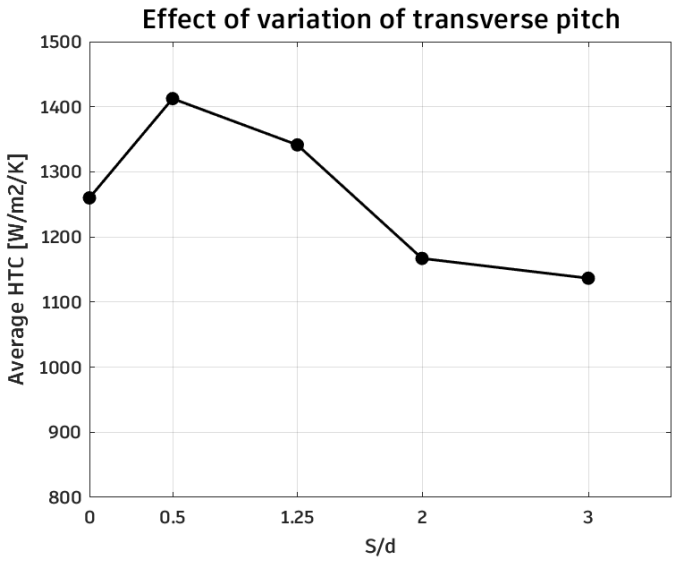

FIGURE 3.24: EFFECT OF TRANSVERSE PITCH VARIATION ON THE AVERAGE HTC

Instead of getting the highest values for average heat transfer coefficient with geometries that have the highest mass flow rate, Figure 3.24 shows different results. The HTC is maximized for the geometry with the transverse pitch of $\frac{S}{d} = 0.5$. The results can be explained with the analysis of the flow field, presented in Figures 3.25 and 3.26, through representations of velocity magnitudes and streamlines. The geometry with transverse pitch $\frac{S}{d} = 2$ forms parallel local flows that pass between the rows of wires, without contributing to the enhancment of heat transfer. Additionally, the flow is mainly formed on one side of the heater. The improvement in the formation of local flows can be noticed for the geometry with the transverse pitch $\frac{S}{d} = 1.25$. Here, the velocity field is more evenly distributed around all wires. The geometry that maximized the average HTC has streamlines practically symmetrical, providing more even heat transfer along the heater. The velocity field formed around each wire aligns with the placement of the adjacent wire, thus enhancing its heat transfer.

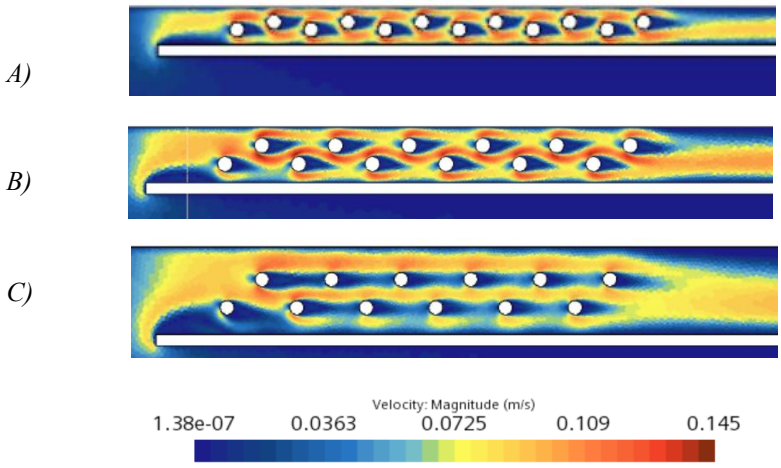

FIGURE 3.25: VELOCITY FIELD OF SALT AROUND WIRES A) $\frac{S_T}{d} = 0.5$ *B)* $\frac{S_T}{d} = 1.25$ *C)* $\frac{S_T}{d} = 2$

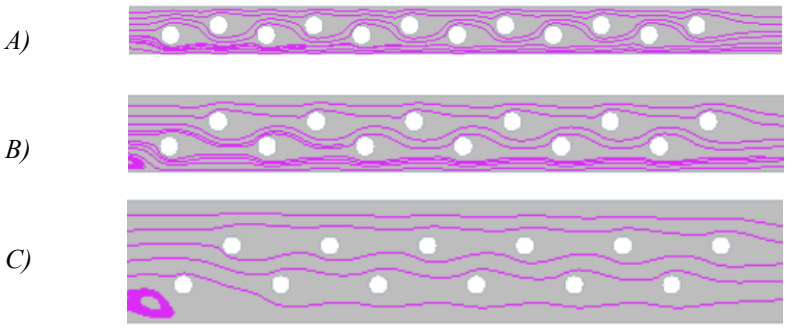

FIGURE 3.26: STREAMLINES AROUND WIRES A) $\frac{S_T}{d} = 0.5$ *B)* $\frac{S_T}{d} = 1.25$ *C)* $\frac{S_T}{d} = 2$

Table 3.4: Effect of transverse pitch variation on maximum salt temperatures

Transverse pitch:	$\frac{S_T}{d} = 0$	$\frac{S_T}{d} = 0.5$	$\frac{S_T}{d} = 1.25$	$\frac{S_T}{d} = 2$	$\frac{S_T}{d} = 3$
$T_{max}[K]$	639	639	643	660	667

Table 3.4 shows the maximum salt temperatures achieved by each analyzed geometry. The minimum peak temperature is achieved with the geometry that maximizes the average HTC. Therefore, the geometry with longitudinal pitch $\frac{S_L}{d} = 5$ and transverse pitch $\frac{S_T}{d} = 0.5$ is chosen for the model of the electric heater with an annular baffle.

4. Results

Results of the thesis include the analysis of the transient behavior of the charging process of the previously described thermocline thermal energy storage by the two configurations of electric heater modeled in paragraph 3.3. The simulations aimed to determine which configuration shows better potential for achieving favorable charging characteristics. These attributes include maintaining a constant temperature during charging at the reference hot temperature of the salt, while also ensuring the inlet temperatures of the channels remain constant at the cold temperature of the salt. Additionally, surface temperatures of the electric resistances are included in the comparison, to decrease the risk of salt decomposition at high temperatures. All models are simulated for the constant heating power corresponding to the peak power of the photovoltaic field ($190kW$).

Initially, the simulation with an imposed constant mass flow rate at the inlet of the channel was carried out. This simulation serves as a reference point on how to achieve good charging characteristics. It determines the value of the constant mass flow rate at which, during one hour of the charging process, the temperatures of salt at the top and the bottom of the tank are maintained at reference hot and cold temperatures, respectively.

Paragraph 4.2 describes the differences in charging transients from two different heater configurations, emphasizing their advantages and disadvantages. Additionally, it presents the outcomes of controlling the mass flow rate during charging using the heater configuration with an annular baffle. This demonstration illustrates the potential of this configuration, by incorporating the benefits of both transient behaviors observed in heaters with flows driven only by buoyancy forces, without mass flow rate control.

Lastly, two methods of mass flow rate control were analyzed with the aim of reaching the transient behavior of the charging process closer to the reference one. The mass flow rate was controlled by dynamic changes of the pressure drop imposed on the fan interface inside the channel.

4.1 Constant mass flow rate charging

To ensure the salt temperature rise of $95K$ (equal to the one of the thermocline prototype – paragraph 1.5) with a constant heating power of $190kW$, electric heater with an annular baffle was simulated with constant charging mass flow rate of $0.2\,\frac{kg}{s}$.

The CFD model includes all characteristics explained in paragraph 3. The thermocline domain was divided into two parts. One part, placed at the bottom of the annular baffle, imposes the inlet boundary condition at constant mass flow rate from one side, and connects to the rest of the domain with an internal interface from the other side. The inlet is characterized also by the constant temperature, set at initial temperature, which is the same as the cold salt temperature. This temperature constraint ensures accurate results as long as the salt near the inlet of the channel stays at the constant cold salt temperature.

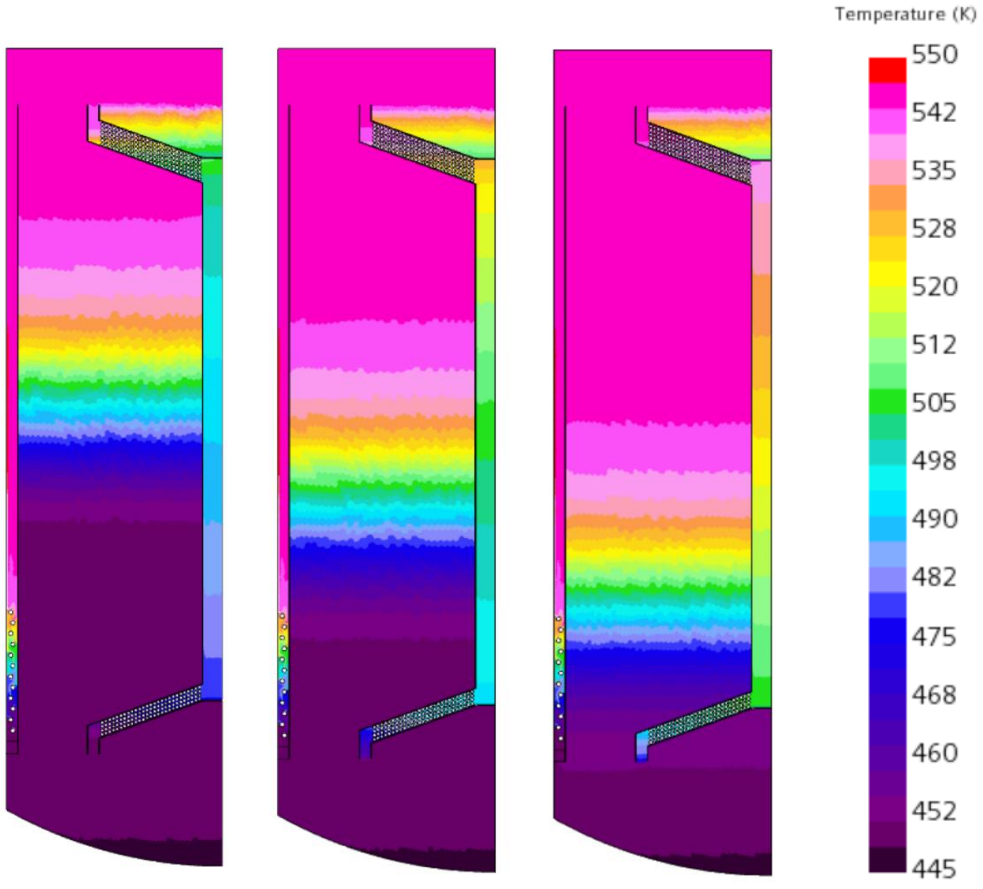

FIGURE 4.1: TEMPERATURE FIELD - CONSTANT MASS FLOW RATE A) $t = 40min$ *B)* $t = 50min$ *C)* $t = 1h$

Figure 4.1 shows temperature distribution of the salt inside the thermocline TES at three different points in time: after 40, 50 and 60 minutes of charging. The dark pink color in the picture represents the hot salt temperature of $546K$, and the light purple color is the cold salt temperature of $450K$. The dark purple color seen at the very bottom of the tank represents the temperature decrease caused by convection losses from the bottom wall. The imposed charging mass flow rate ensured the separation of hot and cold salts, with a thermocline layer in between, which takes up the space of about one fourth of the salt domain. As the charging time increases, more of the domain of the salt reaches the hot salt temperature, and the thermocline layer moves closer to the bottom of the tank, while keeping the same thickness. This is the desirable charging behavior because it ensures good energy quality, and that is why this simulation represents the reference for the behavior we want to achieve for charging transient.

The transient temperature changes for one hour of charging time along the vertical cross section of the tank are presented in Figure 4.2, with temperature measurements at same 4 points used for grid independence study (Figure 3.8). Temperature at different points shows the same trend of the increase from cold to hot salt temperature, with a delay based on their position along the vertical cross section. The temperature in point D, which is the point closest to the channel inlet out of 4 points considered, remains at the initial value for most of the charging time.

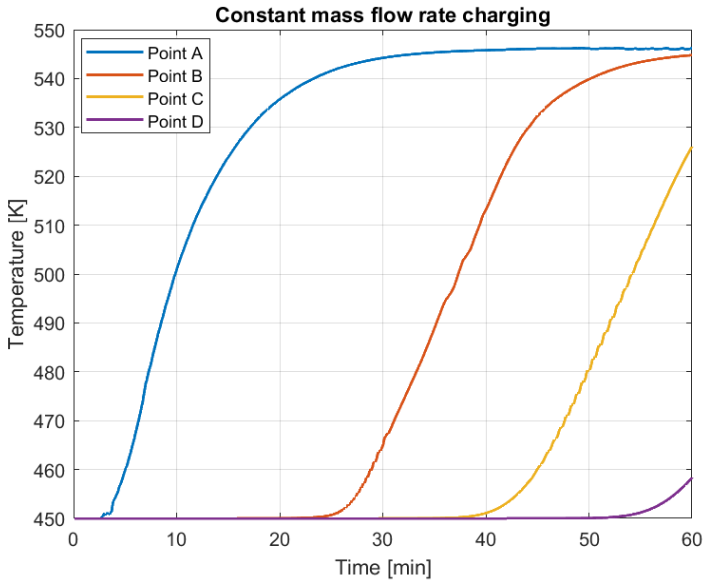

FIGURE 4.2: TRANSIENT TEMPERATURE CHANGE - CONSTANT MASS FLOW RATE

Figure 4.3 shows the transient temperature of the flow exiting the channel. This temperature reaches the desirable value after approximately 15 minutes and remains at steady state for the rest of the charging time. Before reaching this point, the temperature of the salt at the outlet of the channel undergoes fluctuations that do not follow the expected almost linear

trend. These fluctuations are affected by reverse local flows inside the channel, that are caused by buoyancy forces between the layers of fluid at different temperatures (Figure 4.3). Since the mass flow rate of the fluid inside the channel is relatively low, these local buoyancy perturbations have more significance, and they affect the velocity and temperature fields. This effect should be considered for the optimization of the mass flow rate control.

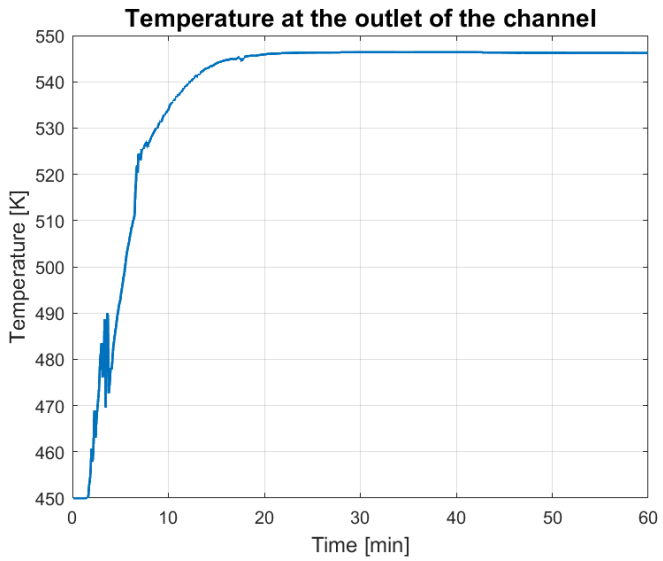

FIGURE 4.3: OUTLET TEMPERATURE TRANSIENT - CONSTANT MASS FLOW RATE

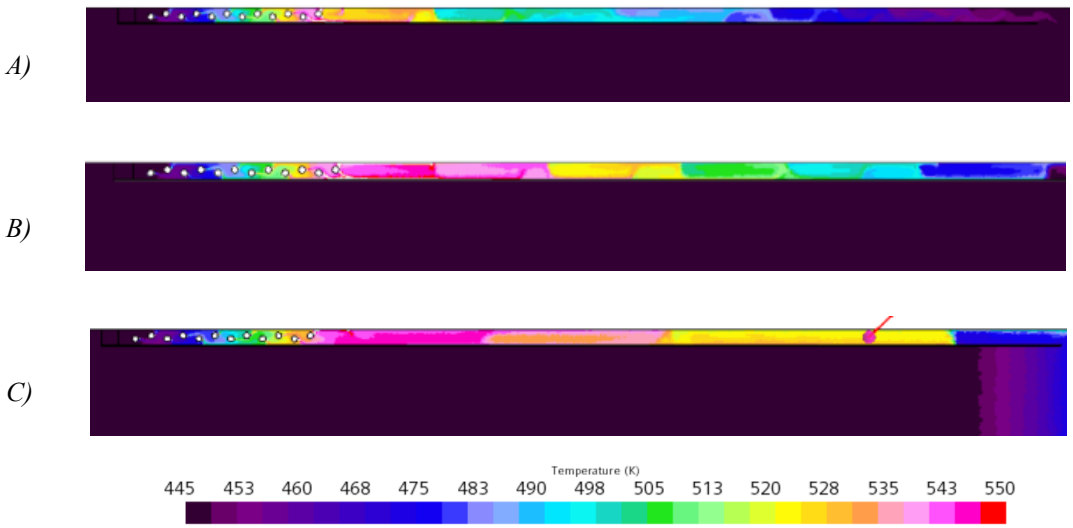

FIGURE 4.4: TEMPERATURE FIELD INSIDE THE CHANNEL – CONSTANT MASS FLOW RATE
A) $t = 150s$ *B)* $t = 230s$ *C)* $t = 450s$

4.2 Comparison of buoyancy-driven charging characteristics between different heater configurations

Two heaters modeled according to the parametric analysis from paragraph 3.3 were simulated for a charging time of 40 minutes. The flows in these simulations are driven only by buoyancy forces and are not controlled in any way. Temperature profiles of the thermocline after the total simulation time are shown in Figure 4.5, and the transient temperatures are represented in Figure 4.6.

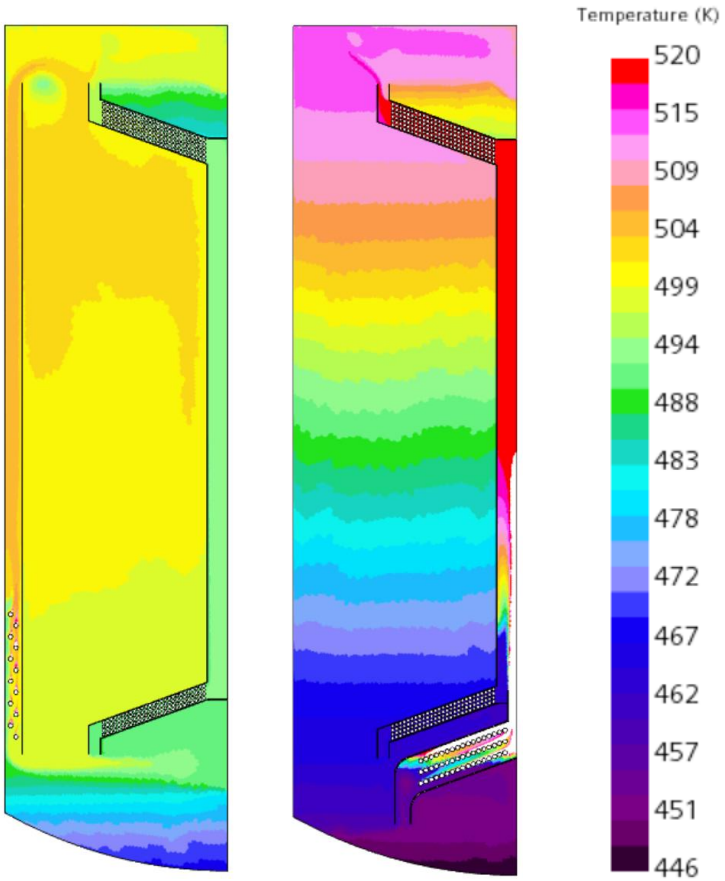

A) *B)*

FIGURE 4.5: TEMPERATURE FIELDS OF BUOYANCY-DRIVEN FLOWS FOR A HEATER CONFIGURATION A) WITH AN ANNULAR BAFFLE B) CONICAL SERPENTINE

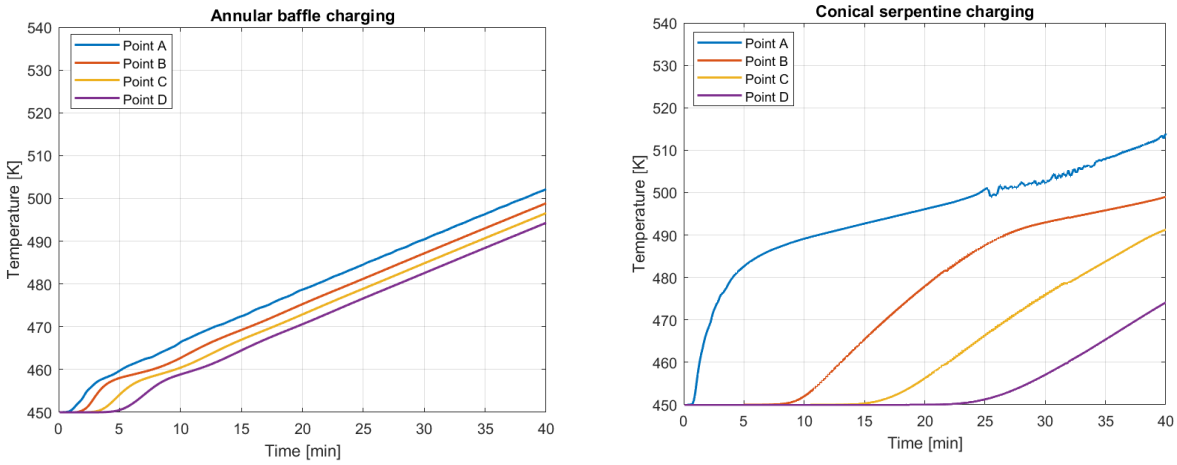

A) *B)*

FIGURE 4.6: TRANSIENT TEMPERATURES OF BUOYANCY-DRIVEN FLOWS FOR A HEATER CONFIGURATION A) WITH AN ANNULAR BAFFLE B) CONICAL SERPENTINE

The temperature profiles of the two configurations show different charging behaviors. Electric heater with an annular baffle does not show temperature stratification. The temperature of most of the domain is at uniform value after 40 minutes of charging. Figure 4.6 a) shows that after approximately 10 minutes of charging, temperatures of all 4 points along the vertical cross-section of the tank start increasing linearly, without reaching the steady state. That is the consequence of the high charging mass flow rate caused by buoyancy forces, that is 8 times higher than the reference mass flow rate for achieving good stratification (Table 4.1). The heated salt quickly circulates from the top of the tank to the bottom and reenters at the channel inlet at a temperature higher than the cold salt temperature. Since the heating is at constant power, the temperature at the outlet of the channel increases linearly. This behavior gives poor energy quality since there is no clear separation between hot and cold salt. The advantage of this profile is the fact that temperatures on the surface of the electric resistances are close to the charging temperature, reducing the risk of salt decomposition.

On the other hand, charging with the conical serpentine electric heater provides temperature stratification along the vertical cross-section of the tank, and better energy quality with higher temperatures at the top of the tank. The charging mass flow rate in this case is closer to the reference one, but still around 50% higher (Table 4.1). The higher mass flow rate results in the same effect of salt reentering the channel at higher temperatures, before allowing the temperatures to reach the steady state. The linear increase of temperatures for this configuration is noticeable after 30 minutes of charging. However, decreasing the charging mass flow rate in this configuration could potentially be risky for salt decomposition since the results show accumulation of high-temperature salt around electric resistances (Figure 4.7 b).

Different temperature ranges are shown in Figures 4.5 and 4.7, for highlighting different aspects of charging characteristics, therefore, the same colors in the figure representing the temperatures of salt around electric resistances correspond to temperatures $40K$ higher than in the figure showing the temperature stratification of the whole tank.

Table 4.1: Charging mass flow rates of buoyancy-driven flows

Configuration	$\dot{m}[\frac{kg}{s}]$
Annular baffle	1.65
Conical serpentine	0.32

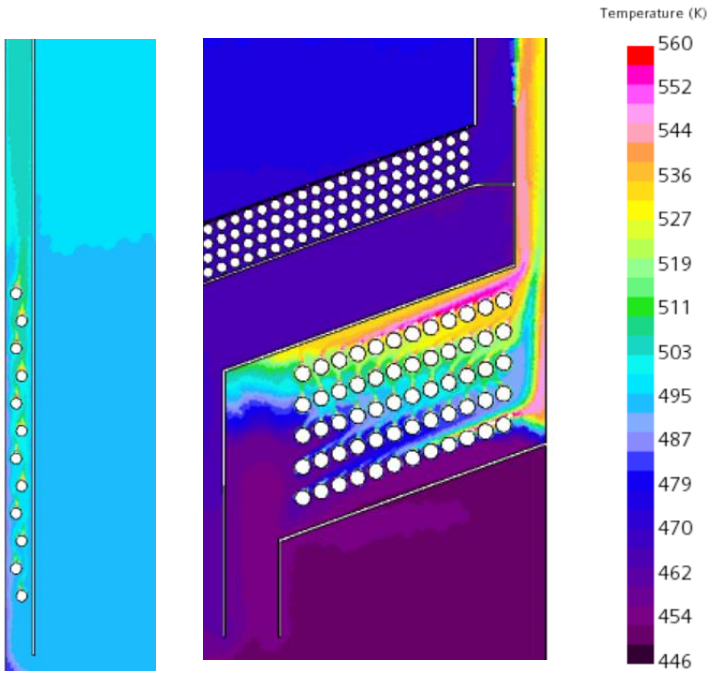

A) B)

FIGURE 4.7: TEMPERATURE FIELD AROUND ELECTRIC RESISTANCES FOR THE HEATER A) WITH AN ANNULAR BAFFLE B) CONICAL SERPENTINE

4.2.1 Potential of heater configuration with an annular baffle

To better compare the two heater models, the electric heater with an annular baffle was simulated with lower charging mass flow rate. By dividing the computational domain in two parts, fan interface is created inside the annular baffle channel to impose a pressure drop that would decrease the charging mass flow rate. For the imposed pressure drop of $300Pa$ the charging mass flow rate was reduced to $0.32\frac{kg}{s}$, which is the value close to the one from the simulation of conical serpentine electric heater. The resulting temperature profile is presented in Figure 4.8 b), along with profiles from previous simulations, with adjusted temperature range, to fit the new simulation better, and have clearer comparison with previous results.

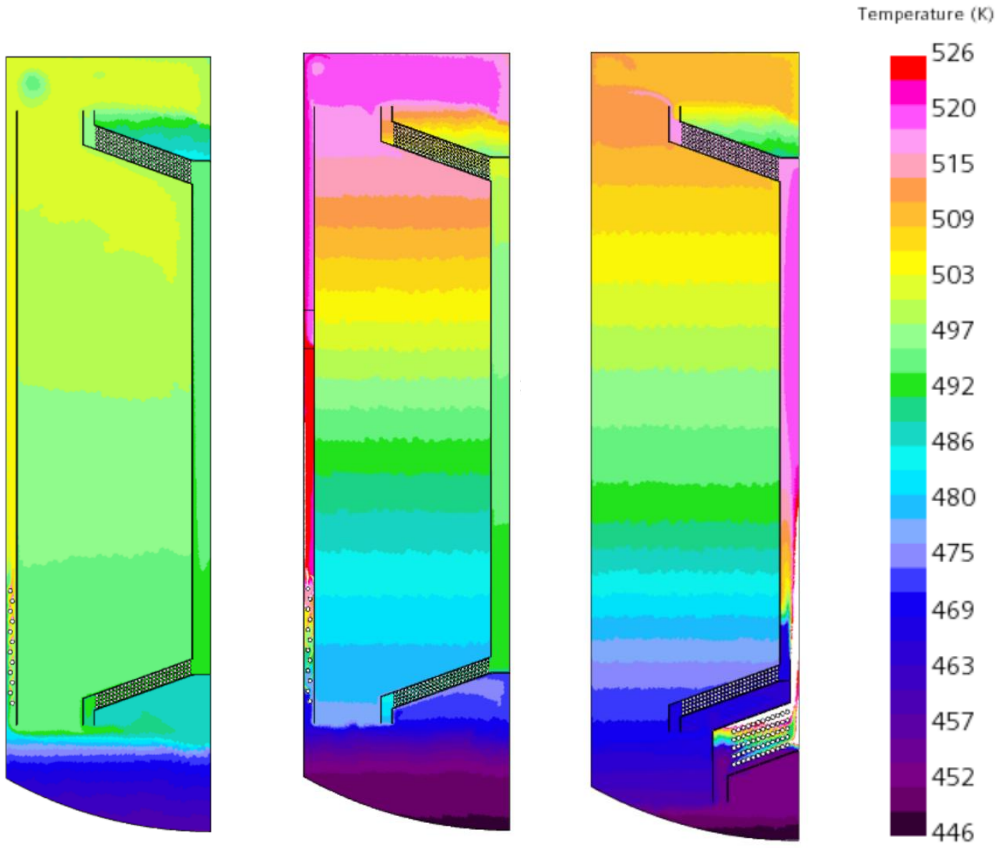

FIGURE 4.8: TEMPERATURE FIELD FOR A HEATER CONFIGURATION A) WITH AN ANNULAR BAFFLE, B) WITH IMPOSED PRESSURE DROP OF 300 PA, C) CONICAL SERPENTINE

Compared to the conical serpentine simulation, with the similar charging mass flow rate, configuration of the electric heater with an annular baffle was able to achieve better energy quality, and higher salt temperatures at the top of the tank, with similar temperature stratification along the vertical cross-section. Additionally, the salt around the heating objects stayed at temperatures close to the charging temperature (Figure 4.9). Table 4.2 shows the maximum surface temperatures achieved in all three simulations. With the imposed pressure drop, the peak temperature increased by only $3K$ compared to the peak temperature of annular baffle charging without mass flow rate control, while providing much better energy quality. These results prove that the electric heater configuration with an annular baffle shows better potential for achieving good charging characteristics than the conical serpentine heater. However, the clear separation of the hot and cold salt was still not achieved. Therefore, more precise mass flow rate control methods are described in the following paragraph.

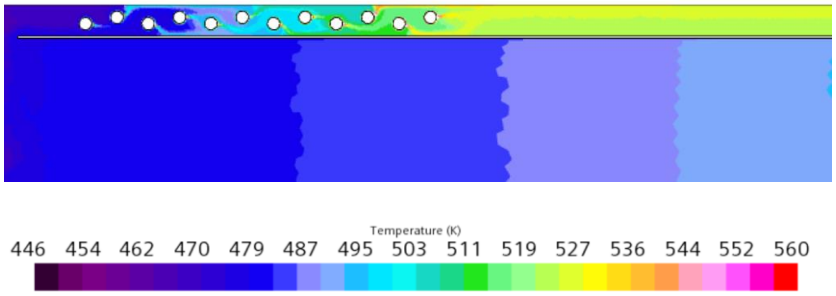

FIGURE 4.9: TEMPERATURE FIELD AROUND ELECTRIC RESISTANCES - IMPOSED PRESSURE DROP OF 300 PA

Table 4.2: Maximum surface temperatures

Configuration	$T_{max}[K]$
Annular baffle (only buoyancy driven)	709
Annular baffle (with 300Pa imposed pressure drop)	712
Conical serpentine	725

4.3 Control of the charging mass flow rate with imposed pressure drop

Since the previous simulations showed that the electric heater with an annular baffle has more potential for achieving good charging characteristics, this model was simulated with the aim of reaching the charging mass flow rate close to the one of the reference case (paragraph 4.1). The mass flow rate was controlled by changing the pressure drop of the fan interface.

Imposed pressure drop of 600 Pa

Increasing the pressure drop further from the previous simulation resulted in the mass flow rate stabilizing at desired value for the pressure drop of 600 Pa. Figures 4.10 and 4.11 show the variations in charging mass flow rate, and the imposed pressure drop changes to achieve the desirable mass flow rate, respectively.

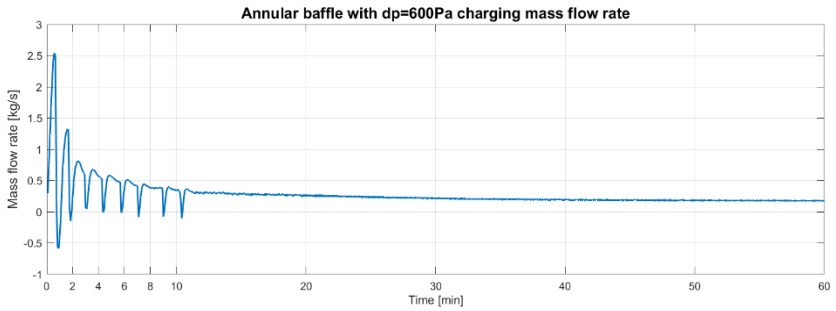

FIGURE 4.10: THE MASS FLOW RATE FLUCTUATIONS - IMPOSED PRESSURE DROP OF 600 PA

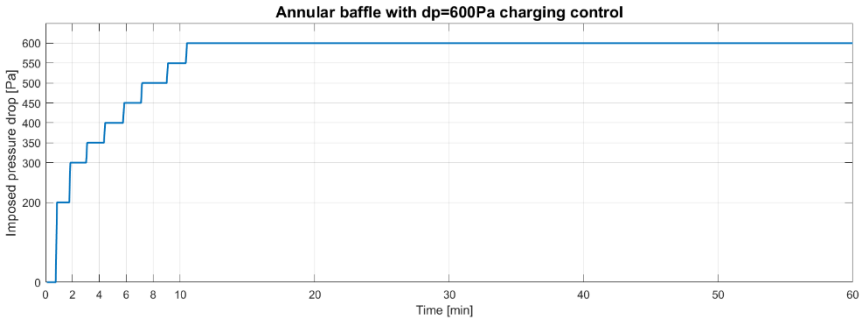

FIGURE 4.11: TRANSIENT PRESSURE DROP CONTROL - IMPOSED PRESSURE DROP OF 600 PA

The pressure drop at the fan interface was imposed after a certain delay, to allow the buoyancy forces to create a flow inside the channel first. If it were imposed in the beginning of the simulation, the fluid would have started flowing in the opposite direction, heating the tank from the bottom. Once the direction of the fluid motion is changed, it takes a long time for buoyancy forces to overweigh and reverse the flow in the right direction. That is why the pressure drop had to be imposed step by step, while making sure that the fluid was moving in the right direction before the stabilization of the mass flow rate. Figure 4.11 shows how the pressure drop was imposed gradually up to $600\ Pa$, and was later kept constant at that value. After the final change in the value of the imposed pressure drop, the charging mass flow rate kept slowly decreasing from $0.3\ \frac{kg}{s}$ around 11^{th} minute, to $0.2\ \frac{kg}{s}$ after approximately 30 minutes of charging, after which it remained nearly constant. After 30 minutes of charging, when the mass flow rate stabilized at the wanted value, the temperature of the salt close to the channel inlet already got heated above the cold salt temperature (point D, Figure 4.12), not leaving enough time for the stabilization of the charging temperature. According to the reference simulation from the paragraph 4.1, it takes a significant amount of time for the charging temperature to reach the steady state at the constant mass flow rate charging, and to achieve it, the inlet temperature must be kept constant in that transient period. Before the mass flow rate stabilized at $0.2\ \frac{kg}{s}$, temperature field was already highly influenced by the higher values of charging mass flow rate. Therefore, the desired charging behavior was not met with the control method presented in Figure 4.11. After 40 minutes of charging, the salt at the inlet of the channel has already increased its temperature, while the salt at the top of the tank has still not reached the reference hot salt temperature (Figure 4.13 – temperature range in the picture the same as the one of the reference case, for clearer comparison).

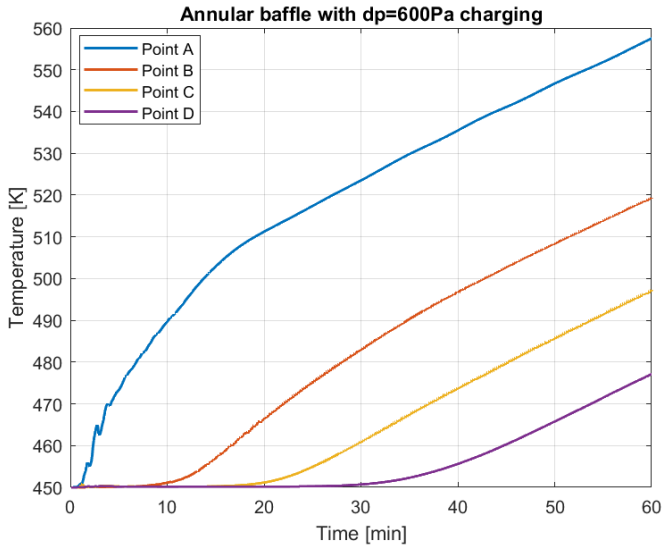

FIGURE 4.12: TRANSIENT TEMPERATURE - IMPOSED PRESSURE DROP OF 600PA

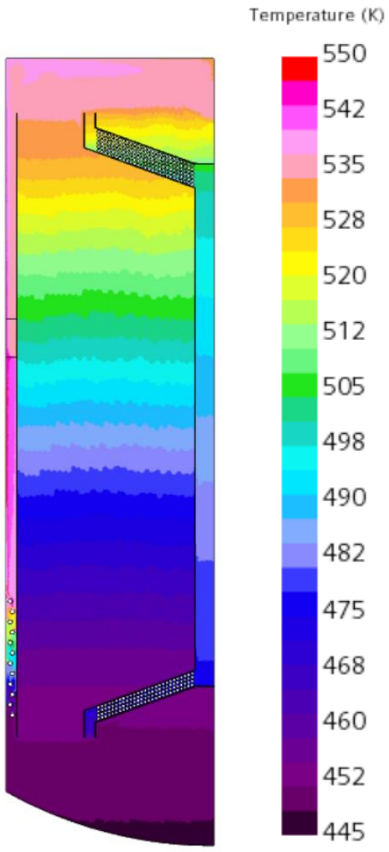

FIGURE 4.13: TEMPERATURE FIELD AFTER 40 MINUTES OF CHARGING - IMPOSED PRESSURE DROP OF 600 PA

Dynamic control of the charging mass flow rate

The previous simulation showed that mass flow rate needs to reach the desired value sooner to avoid the formaion of a large thermocline that prevents the charging temperature to reach the steady state. In a new attempt to achieve the good charging transient, pressure drop was first imposed gradually up to 800 Pa, which provided the mass flow rate close to 0.2 $\frac{kg}{s}$ after approximetly 18 minutes of charging. Again, in this case, the pressure drop was increased gradually to prevent the fluid flow inside the channel to form in the opposite direction. The previous simulation also showed that mass flow rate slowly decreases to reach the steady state after the last pressure change is imposed. That is why, after imposing the pressure drop of 800 Pa, it needed to gradually decrease to keep the mass flow rate at wanted value (Figures 4.15). Therefore, after 18 minutes, the pressure drop was varied from 800 Pa to 475 Pa, which allowed the mass flow rate to stay in the range of $\pm 10\%$ from the required value. Exceptions

were the mass flow rate peaks caused by imposing a step function in pressure drop, because of an instantanious change in the control (Figure 4.14).

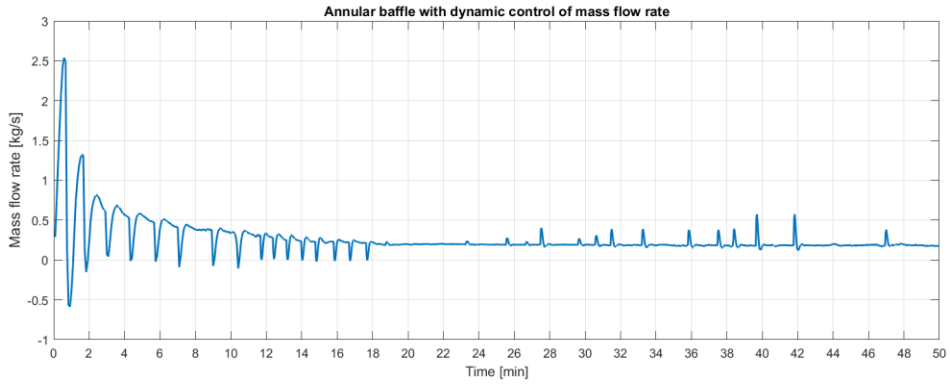

FIGURE 4.14: THE MASS FLOW RATE FLUCTUATIONS – DYNAMIC CONTROL OF PRESSURE DROP UP TO 800PA

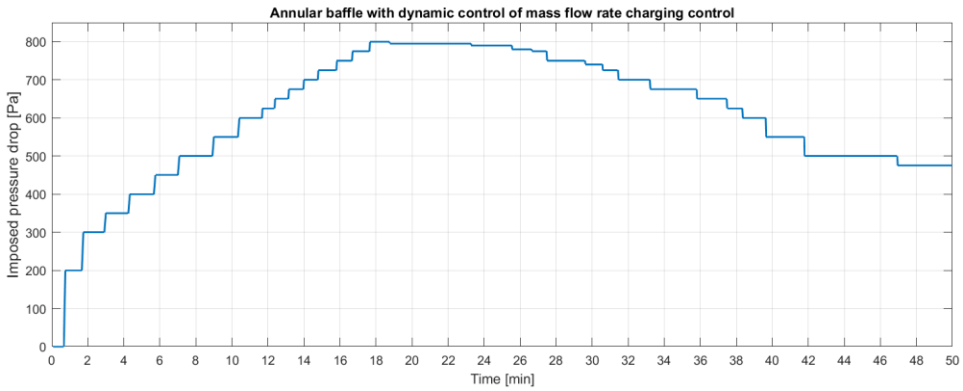

FIGURE 4.15: TRANSIENT PRESSURE DROP CONTROL – DYNAMIC CONTROL OF PRESSURE DROP UP TO 800PA

The resulting charging transient shows promising potential (Figures 4.16 and 4.17). After 40 minutes of charging, the temperature field is comparable with the reference case one. The layer of the salt at the top reached a temperature close to the hot salt temperature, while the salt near the channel inlet stayed at the initial temperature. The difference is the thickness of the thermocline layer, that in this case takes up most of the salt volume. In the first 20 minutes, the charging mass flow rate varied drastically, with large amplitudes, before reaching the desired value. During this period, a large thermocline layer was already created, and the salt at a temperature higher than the initial one already reached the bottom third of the salt domain. After approximately 45 minutes of charging, the heated salt already reached the channel inlet,

and it caused the outlet temperature of the channel to continue increasing linearly instead of maintaining the steady state value. Figure 4.16 c) shows that after 50 minutes of charging, the temperature inside the channel continued increasing (white color indicates the temperature outside the defined range, which means that salt was heated to a temperature higher than 550 K). Figure 4.17 shows that the point A, which is the point in the domain closest to the top of the tank, reaches a steady state around 40 minutes of charging, but, as the inlet temperature starts increasing, also the temperature of point A starts to show linear trend after 45 minutes.

These results show that the control method of mass flow rate needs to be optimized in a way that would allow it to reach the desired value sooner and stay in a reasonable offset without peaks for the rest of the charging. This would require dynamic control of the pressure drop with optimized damping coefficient, to avoid the peaks caused by the sudden changes that come with imposing a step function for pressure drop.

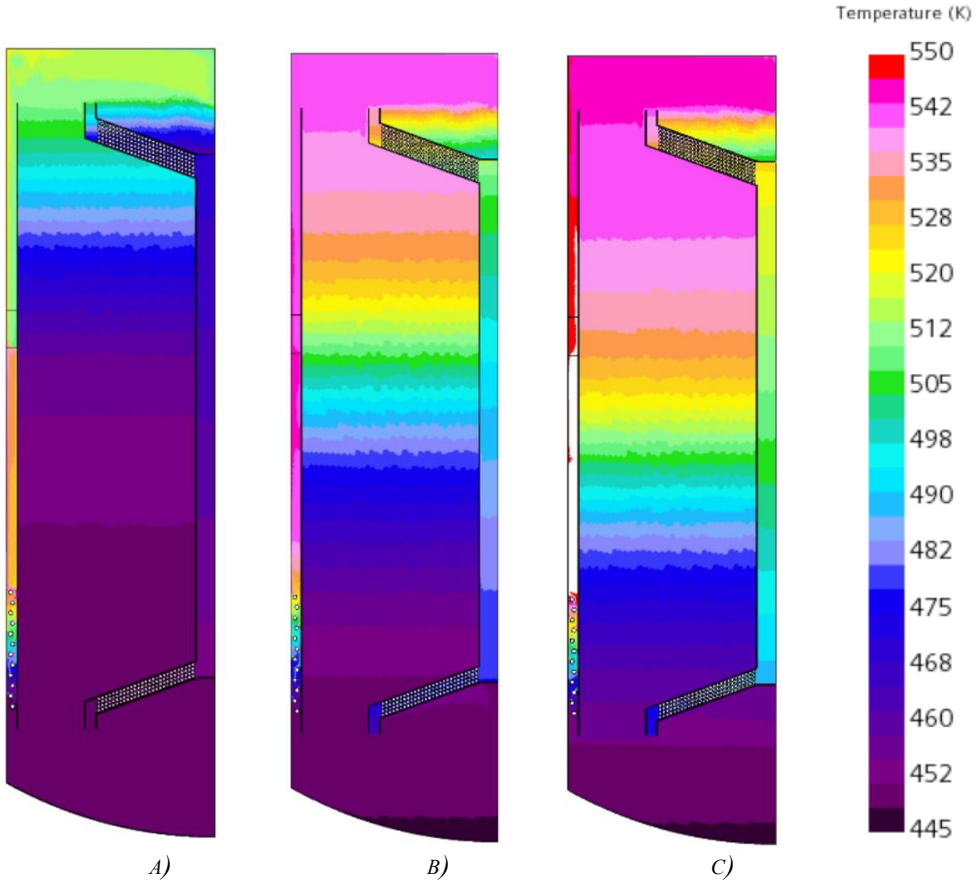

FIGURE 4.16: TEMPERATURE FIELD – DYNAMIC CONTROL OF PRESSURE DROP UP TO 800PA
A) $t = 20min$ *B)* $t = 30min$ *C)* $t = 50min$

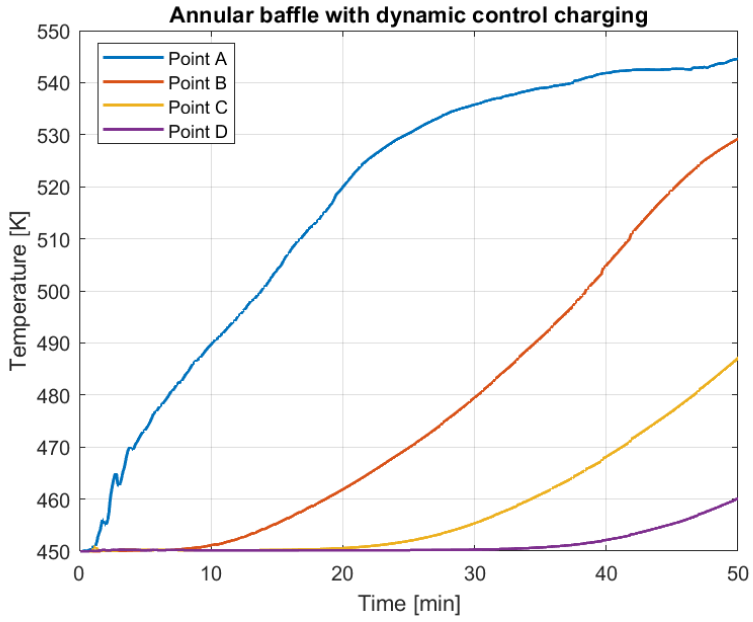

FIGURE 4.17: TRANSIENT TEMPERATURE – DYNAMIC CONTROL OF PRESSURE DROP UP TO 800PA

5. Conclusions and perspectives

The contribution of the research presented in this thesis is summarized in the following points:

- The numerical model was developed for a thermocline thermal energy storage unit that is a connecting element in the hybridization of CSP and PV solar technologies. That means that the model includes a charging and a discharging heat exchanger for the heating from the CSP field, as well as an immersed electric heater for storing the electricity produced by the PV field.

- For the design of the immersed electric heater, two different configurations were analyzed: a conical serpentine model, sharing a channel with the existing CSP charger, and an electric heater with an annular baffle. For both configurations, parametric analysis, which considered different patterns of wires, was used to maximize the heat transfer coefficient. Based on the results of these studies, two final electric heater models were chosen: for conical serpentine the HTC was maximized for longitudinal and transverse pitches of $\frac{S_L}{d} = 1.25$ and $\frac{S_T}{d} = 2$, while for the heater with an annular baffle the chosen parameters are $\frac{S_L}{d} = 5$ and $\frac{S_T}{d} = 0.5$.

- The thermocline CFD model was simulated with constant charging mass flow rate, allowing the charging temperature to reach a steady state. The results of this simulation showed good charging characteristics, and a temperature field with

clearly separated hot and cold salt parts, divided by the thermocline. It allowed the constant temperature rise of $95K$, which was the design parameter. After one hour of charging, half of the salt domain was charged at the hot salt temperature. This simulation served as a reference for the desired charging behavior.

- Both models of the electric heater were simulated with the fluid flow affected only by buoyancy forces for a total time of charging of 40 minutes. From these simulations, it was shown that conical serpentine electric heater causes better temperature stratification and provides better energy quality. However, it creates zones around the electric resistances at a temperature much higher than the charging one. This increases the risk of reaching temperatures of salt thermal decomposition. On the other hand, the electric heater with an annular baffle provides surface temperatures of the electric resistances close to the charging temperature, but does not provide thermal stratification, because of the high charging mass flow rate.

- To better compare the two configurations, the electric heater with an annular baffle was simulated with the decreased charging mass flow rate to match the value reached by the natural convection around conical serpentine heater. This was done by imposing the pressure drop of $300Pa$ inside the channel. The results demonstrated that the configuration with an annular baffle shows better potential for reaching good charging characteristics, since it creates better stratification and energy quality than the conical serpentine heater, for the same charging mass flow rate, while at the same time keeping temperatures around resistances low.

- The mass flow rate of the heater with an annular baffle was controlled by the dynamically changing imposed pressure drop to reach the value of the reference simulation. This was done in two ways: by imposing the maximum pressure drop of $600Pa$ and keeping it constant until the end of the simulation, and by imposing the maximum pressure drop of $800Pa$ and gradually decreasing it to keep the mass flow rate constant. The second attempt showed results more similar to the reference simulation. However, to further improve the transient characteristics, the charging mass flow rate control needs to be optimized to reach the desired value sooner and keep it close to the constant value until the end of the charging period.

- The research set references for the control of the charging process from the electric heater at peak power operation from the photovoltaic field.

Perspectives for future research based on the results obtained in this thesis are:

- The numerical model should be simulated for different imposed heat flux values on the walls of electric resistances corresponding to lower power generation from the PV field, to understand the behavior of the system in real operating conditions during the whole cycle and adapt the mass flow rate control accordingly.

- Considering that both CSP and PV fields use solar energy as a resource, the storage tank unit would be charged simultaneously with both heaters at certain periods of time. That is why the model should be simulated with heat fluxes imposed on the walls of both electric heater and CSP charging heat exchanger, to understand how the temperature field of the tank is affected by simultaneous charging. The charging mass flow rate control for both channels should be adapted accordingly, considering the different operating conditions of the hybrid plant.

Nomenclature

CFD – Computational Fluid Dynamics

CSP – Concentrated Solar Plant

DNS – Direct Numerical Solution

Ge – Gebhart number

GHG – Greenhouse Gases

HSM – Heat Storage Medium

HTC – Heat Transfer Coefficient

HTF – Heat Transfer Fluid

LCOE – Levelized Cost of Energy

LES – Large Eddy Simulation

Nu – Nusselt number

ORC – Organic Rankine Cycle

PDE – Partial Differential Equation

Pr – Prandtl number

PV – Photovoltaic

Ra – Rayleigh number

RANS – Reynolds-Averaged Navier-Stokes

Re – Reynolds number

RES - Renewable Energy Sources

SDG – Sustainable Development Goals

TES – Thermal Energy Storage

List of figures

List of tables

References

[1] W. K. Darkwah et al. (2018) “Greenhouse Effect: Greenhouse Gases and Their Impact on Global Warming”. Journal of Scientific Research and Reports, 17. 1-9.

[2] Center for Sustainable Systems, University of Michigan. (2023) “Climate Change: Science and Impacts Factsheet.” Pub. No. CSS05-19

[3] Climate Watch (2023) – with major processing by Our World in Data. “Agriculture” [dataset]. Climate Watch, “Greenhouse gas emissions by sector”

[4] United Nations (2015) “Transforming our world: the 2030 Agenda for Sustainable Development”

[5] Edrisian et al. (2013). “The New Hybrid Model of Compressed Air for Stable Production of Wind Farms”, International Journal of Emerging Technology and Advanced Engineering, 3. 37-43.

[6] International Renewable Energy Agency (2023) – with minor processing by Our World in Data

[7] Gedle, Yibekal & Schmitz, Mark & Merige, Phani & Teixeira Boura, Cristiano José & Mahdi, Zahra & Chico Caminos, Ricardo & Dersch, Jürgen. (2020) “Analysis of an Integrated CSP-PV hybrid power plant”

[8] Guruprasad Alva, Yaxue Lin, Guiyin Fang. (2018) “An overview of thermal energy storage systems”, Energy, Volume 144 Pages 341-378, ISSN 0360-5442

[9] Yin, Jun-Ming & Zheng, Qiu-Yun & Zhang, Xin-Rong. (2019) “Heat transfer model of a particle energy storage based moving packed bed heat exchanger. Energy Storage”. 2. 10.1002/est2.113.

[10] Falchetta, Massimo & Binotti, Marco & Avallone, Fabrizio. (2019) “Modelling thermocline storage for CSP yield assessment and process control simulation”. AIP Conference Proceedings. 2126. 200018. 10.1063/1.5117733.

[11] Marc A Rosen (2001) “The exergy of stratified thermal energy storages”, Solar Energy, Volume 71, Issue 3, Pages 173-185, ISSN 0038-092X,

[12] Alberto Pizzolato, Filippo Donato, Vittorio Verda, Massimo Santarelli. (2015) “CFD-based reduced model for the simulation of thermocline thermal energy storage systems”, Applied Thermal Engineering, Volume 76, Pages 391-399, ISSN 1359-4311

[13] ORC-PLUS (online) Available: https://www.orc-plus.eu

[14] Valeria Russo, Domenico Mazzei, Raffaele Liberatore. (2018) “Thermal energy storage with integrated heat exchangers using stratified molten salt system for 1 MWe CS”, AIP Conf. Proc.; 2033 (1): 090025.

[15] Liberatore, Raffaele & Falchetta, Massimo & Gaggioli, W. & Mazzei, Domenico & Russo, Valeria. (2019) “Power production of an ORC system using a stratified molten salt as thermal energy storage integrated in a CSP plant”, AIP Conference Proceedings. 2126. 140003. 10.1063/1.5117651.

[16] Gaggioli, W. & Liberatore, Raffaele & Ascenzi, Primo & Mazzei, Domenico & Russo, Valeria. (2020) "Experimental test of characterization of an innovative thermal energy storage system based on low melting molten salt thermocline tank integrated with an oil exchanger", AIP Conference Proceedings. 2303. 190012. 10.1063/5.0028779.

[17] Cagnoli, Mattia & Gaggioli, W. & Liberatore, Raffaele & Russo, Valeria & Zanino, Roberto. (2023) "CFD modelling of an indirect thermocline energy storage prototype for CSP applications", Solar Energy. 259. 86-98. 10.1016/j.solener.2023.05.019.

[18] H. K. Versteeg and W. Malalasekera. (2007) "An Introduction to Computational Fluid Dynamics - The finite volume method", Pearson Education Limited.

[19] Lappa, Marcello. (2022). "Incompressible Flows and the Boussinesq Approximation: 50 years of CFD", Comptes Rendus Mecanique. 350. 10.5802/crmeca.134.

[20] Kimura, Shigeo and Adrian Bejan. (1984) "The boundary layer natural convection regime in a rectangular cavity with uniform heat flux from the side" Journal of Heat Transfer-transactions of The Asme 106: 98-103.

[21] Theodore L. Bergman, Adrienne S. Lavine, Frank P. Incropera, David P. De Witt. (2011) "Fundamentals Of Heat And Mass Transfer", Seventh Edition John Wiley & Sons, Inc.

[22] Yuanwei, lu & Yu, Qiang & Du, Wenbin & Wu, Yuting. (2016) "Natural convection heat transfer of molten salts around a vertically aligned horizontal cylinder set", International Communications in Heat and Mass Transfer. 76. 10.1016/j.icheatmasstransfer.2016.04.022.

[23] Yuanwei, lu & Li, XiaoLi & Li, Qiang & Wu, Yuting & Ma, ChongFang. (2013) "Numerical simulation and experimental investigation of natural convection heat transfer of molten salt around fine wire", Science China Technological Sciences. 56. 10.1007/s11431-013-5253-y.

[24] Nicodemus, Julia & Smith, Joshua & Goldstein, Hannah. (2019) "Numerical simulations of storage-side natural convection to an immersed coiled heat exchanger with baffle-shrouds", Solar Energy. 182. 304-315. 10.1016/j.solener.2019.01.069.

[25] Nicodemus, Julia & Davidson, Jane. (2009) "Discharge of a thermal storage tank using an immersed heat exchanger with an annular baffle", Solar Energy - SOLAR ENERGY. 83. 193-201. 10.1016/j.solener.2008.07.017.

[26] Logie, William & Frank, Elimar. (2013) "A Transient Immersed Coil Heat Exchanger Model", Journal of Solar Energy Engineering. 135. 041006. 10.1115/1.4023928.

[27] Izadpanah, Ehsan & Zarei, Ahmad & Akhavan, Saeed & Babaie Rabiee, Marzie. (2018) "An experimental investigation of natural convection heat transfer from a helically coiled heat exchanger", International Journal of Refrigeration. 93. 10.1016/j.ijrefrig.2018.06.008.

[28] Menter, F. R. (1994) "Two-equation eddy-viscosity turbulence models for engineering applications", AIAA Journal, 32(8), 1598–1605. https://doi.org/10.2514/3.12149

[29] Churchill, Stuart Winston and M. Bernstein (1977) "A Correlating Equation for Forced Convection From Gases and Liquids to a Circular Cylinder in Crossflow", Journal of Heat Transfer-transactions of The Asme 99: 300-306.

[30] Watt Density & Sheath Selection (online) Available:
http://heaters.heatrex.com/Asset/Watt_Density_Sheath_Selection.pdf

[31] Giaconia, Alberto & Tizzoni, Anna & Sau, Salvatore & Corsaro, Natale & Mansi, Emiliana & Spadoni, Annarita & Delise, Tiziano. (2021) "Assessment and Perspectives of Heat Transfer Fluids for CSP Applications", Energies. 14. 7486. 10.3390/en14227486.

[32] Wang, You-Qin & Penner, L. & Ormiston, Scott. (2000) "Analysis of Laminar Forced Convection of Air for Crossflow in Banks of Staggered Tubes", Numerical Heat Transfer Part A - Applications. 38. 819-845. 10.1080/104077800457449.